JUL 2 1 1982

105LH Y3.N88:25/2620

NUREG/CR-2620
EGG-2181

ORIGINAL
COMPLETED

U.S. Department of Energy
Idaho Operations Office • Idaho National Engineering Laboratory

An Analysis of Proposed BWR Inlet Flow Blockage Experiments Using MAYU-4b

41

M. E. Nissley
R. R. Gay
R. T. Lahey, Jr.

MICROFILMED FROM BEST AVAILABLE COPY

May 1982

Prepared for the
U.S. Nuclear Regulatory Commission
Under DOE Contract No. DE-AC07-76IDO1570

EG&G Idaho

NOTICE

This report was prepared as an account of work sponsored by an agency of the United States Government. Neither the United States Government nor any agency thereof, nor any of their employees, makes any warranty, expressed or implied, or assumes any legal liability or responsibility for any third party's use, or the results of such use, of any information, apparatus, product or process disclosed in this report, or represents that its use by such third party would not infringe privately owned rights.

Available from

GPO Sales Program
Division of Technical Information and Document Control
U.S. Nuclear Regulatory Commission
Washington, D.C. 20555

and

National Technical Information Service
Springfield, Virginia 22161

NUREG/CR-2260
EGG-2181
Distribution Category: R3

AN ANALYSIS OF PROPOSED BWR INLET FLOW BLOCKAGE EXPERIMENTS USING MAYU-4b

M. E. Nissley[a]
R. R. Gay[a]
R. T. Lahey, Jr.[a]

Published May 1982

EG&G Idaho, Inc.
Idaho Falls, Idaho 83415

Prepared for the
U.S. Nuclear Regulatory Commission
Washington, D.C. 20555
Under DOE Contract No. DE-AC07-76IDO1570
FIN No. A6041

a. Department of Nuclear Engineering, Rensselaer Polytechnic Institute, Troy, New York 12181.

ABSTRACT

The purpose of this report is to present an analytical study of hypothetical boiling water reactor (BWR) inlet flow blockage accidents. To this end, MAYU-4, a one-dimensional drift-flux digital computer code, was modified to account for nonequilibrium vapor generation, radiation heat transfer, rod bundle countercurrent-flow-limited phenomena, and the exothermic metal-water reaction of the cladding. The revised code, MAYU-4b, was used to investigate postulated BWR inlet flow blockage events and the feasibility of such testing in the Power Burst Facility (PBF) at the Idaho National Engineering Laboratory. It was found that, due to the relatively short length of the PBF core (3 ft), simulation of all facets of a BWR inlet flow blockage event would be difficult. Nevertheless, it may be possible to gain valuable information on fuel failure propagation and the potential for vapor explosions in the PBF.

SUMMARY

This report presents the results of a study of boiling water reactor (BWR) inlet flow blockage accidents. In particular, the thermal-hydraulic response of a blocked BWR fuel rod bundle was simulated, and the suitability of using the Power Burst Facility (PBF) at the Idaho National Engineering Laboratory for such experiments was investigated.

A major blockage of the inlet orifice and/or lower tie plate of a BWR fuel rod bundle may result in failed fuel rods, and molten fuel and cladding. The safety concern is that a molten fuel/cladding mixture may penetrate the channel wall, resulting in fuel failure propagation, only partial control rod insertion, and/or mechanical damage due to a vapor explosion. Unfortunately, little is known about the actual scenario.

To more throughly investigate the consequences of such an accident, a study was performed for EG&G Idaho, Inc., to determine the suitability of the PBF to conduct inlet flow blockage simulations. To this end, an advanced, one-dimensional drift-flux digital computer code (MAYU-4b) was developed and used. This code accounted for nonequilibrium vapor generation (i.e., vapor superheat), radiation heat transfer, rod bundle countercurrent flow phenomena, and the exothermic metal-water reaction of the cladding.

Analyses using MAYU-4b indicated that, because of leakage inflow to a completely blocked BWR fuel rod bundle, there will be a countercurrent-flow-limited (CCFL) condition at the upper tie plate which prevents liquid fallback from the upper plenum. Moreover, it was found that because of the shorter heated length of the PBF core (3 ft), compared to a BWR core (12 ft), the exit vapor superheat would be less in the PBF. This affects the core exit velocity (and thus CCFL) and the core heatup rate.

It appears that it would be difficult to completely simulate a BWR inlet flow blockage accident in the PBF. Nevertheless, it may be possible to use the PBF to gain valuable information on the potential for fuel failure propagation and/or vapor explosions.

ACKNOWLEDGMENTS

The authors wish to thank Mr. Katsu Ohkawa and Mr. Cal Hardie for their extensive preliminary work and assistance. Also, the excellent typing by Regina LaHait and the assistance provided by Marilyn Mamone and Peg Barnes is greatly appreciated.

CONTENTS

ABSTRACT ii

SUMMARY iii

ACKNOWLEDGMENTS iv

NOMENCLATURE vii

INTRODUCTION 1

CODE DESCRIPTION 2

- Conservation Equations 2
- Drift-Flux Parameters 4
- One-Dimensional Radial Heat Conduction Model 5
- Metal-Water Reaction Model 9
- Thermal Limits Correlations 10
- Heat Transfer Correlations 11

NONEQUILIBRIUM VAPOR GENERATION 14

- Nonequilibrium Vapor Generation Model 15
- Calculation of Superheated Vapor Enthalpy in the PDO Regime 17
- Model Verification 18

RADIATIVE HEAT TRANSFER 21

- Radiative Heat Transfer Model 21
- Radiation Model Verification 23

BWR INLET FLOW BLOCKAGE SIMULATION 26

PARAMETRIC RUNS AND RESULTS 31

SUMMARY AND CONCLUSIONS 40

REFERENCES 41

APPENDIX A—ADDITIONAL INPUT AND CHANGES IN INPUT A-1

APPENDIX B—DERIVATION OF THE CONSERVATION EQUATIONS B-1

APPENDIX C—ROD GROUPING C-1

APPENDIX D—SAMPLE OUTPUT D-1

APPENDIX E—PROGRAM LISTING E-1

NOMENCLATURE

A_{HT}	Heat transfer area
A_{xs}	Cross-sectional flow area
B_k	Radiosity of surface-k
c_p	Specific heat at constant pressure
C_o	Void concentration parameter
D_H	Hydraulic diameter
$e_b(T)$	Planck's function evaluated at temperature T
F_{k_j}	Radiation view factor
G	Mass flux
g	Gravitational acceleration
g_c	Gravitational conversion factor
h	Enthalpy
$H_{v\text{-}d}$	Vapor-to-droplet heat transfer coefficient
H_∞	Cladding surface heat transfer coefficient
J	Mechanical equivalent of heat
j_g	Volumetric flux of vapor phase
j_f	Volumetric flux of liquid phase
j	Volumetric flux of two-phase mixture
κ	Thermal conductivity
L_B	Boiling length
L_H	Heated length
N_d	Droplet density
$\dot{N}_d$	Droplet flux
p	Pressure
P_H	Heated perimeter
q''	Total heat flux to fluid

$(q_\ell)_{rad}$	Heat rate to droplets by radiation
$(q_v)_{rad}$	Heat rate to vapor by radiation
q_j'', q_R''	Net surface radiative heat flux
q_v''	Total heat flux to vapor
$q_{v\text{-}d}''$	Convective heat flux from vapor to droplets
q'''	Volumetric heat generation rate
$q'''_{Zr\text{-}H_2O}$	Volumetric heat generation rate due to exothermic zircaloy/water reaction
r	Radial coordinate
T	Temperature
t	Time
u_k	Velocity of phase-k
V_{gj}	Drift velocity
w	Mass flow rate
$<x>$	Flow quality
x_c	Critical quality
x_e	Equilibrium quality
z	Axial coordinate
$<\alpha>$	Void fraction
δ	Droplet diameter
δ_{ik}	$\begin{cases} 1, & i=k \\ 0, & \text{otherwise} \end{cases}$
$\epsilon^{L}_{k_j}$	Liquid emissivity between surfaces k and j
$\epsilon^{v}_{k_j}$	Vapor emissivity between surfaces k and j
Γ	Total volumetric vapor generation rate
Γ_p	Vapor generation rate due to pressure changes
Γ_{rad}	Vapor generation rate due to radiative heat transfer to droplets
ρ	Density

σ	Surface tension, or Stefan-Boltzmann constant
τ_{k_j}	Transmissivity
μ	Dynamic viscosity
$< >$	Area-averaged variable

Subscripts

C_L	Fuel centerline
DO	Dryout
f	Saturated liquid
g	Saturated vapor
ℓ	Liquid phase
sat	Saturation
v	Vapor phase
v-d	Vapor-to-droplet
v-w	Vapor-to-channel wall
w	Wall or surface

AN ANALYSIS OF PROPOSED BWR INLET FLOW BLOCKAGE EXPERIMENTS USING MAYU-4b

INTRODUCTION

The nuclear industry has long been involved in extensive efforts to quantify the consequences of hypothetical light water reactor (LWR) accidents. An important LWR accident is the postulated inlet flow blockage of a boiling water reactor (BWR) fuel rod bundle. A major blockage of the inlet orifice, and/or lower tie plate, of a BWR fuel rod bundle may result in failed fuel rods, and molten fuel and cladding. The safety concern is that the molten fuel/cladding mixture may penetrate the channel wall, resulting in fuel failure propagation, restriction to control rod insertion, and/or mechanical damage due to a vapor explosion. Unfortunately, little is known about the actual scenario.

In order to more thoroughly investigate the consequences of such an accident, the USNRC has been considering in-core inlet flow blockage experiments in the Power Burst Facility (PBF) at the Idaho National Engineering Laboratory. The purpose of the study presented herein is to appraise the suitability of PBF to conduct realistic BWR inlet flow blockage experiments. The study included the development of an appropriate transient thermal-hydraulic analysis capability (MAYU-4b) and its application to BWR inlet flow blockage accidents. A one-dimensional drift-flux digital computer code, MAYU-4,[1] was modified to account for nonequilibrium vapor generation (i.e., vapor superheat), radiation heat transfer, the exothermic metal-water reaction of the cladding, and rod bundle countercurrent-flow-limiting (CCFL) phenomena. The latter (CCFL) model was developed in a previous study.[2]

Since the PBF only has a 3-ft core (compared to a 12-ft core in a BWR), parametric MAYU-4b runs were made with 12- and 3-ft cores to quantify the effect of heated length on the thermal-hydraulic scenario. In addition, particular care was taken to determine the effect of possible liquid fallback from the upper plenum. Indeed, the study was centered on answering the following questions: "How much cooling will occur due to liquid fallback," and, "Can the thermal and mechanical behavior of blocked BWR fuel be adequately simulated in the PBF?"

The report has been organized along the lines of the work conducted. That is, the development and assessment of MAYU-4b is presented first. Next, the MAYU-4b simulation of a BWR inlet flow blockage accident is presented. Parametric inlet flow blockage runs of the thermal-hydraulic response of a PBF-length core (3 ft), and a BWR-length core (12 ft), are then presented. Finally, a summary and the salient conclusions of this study are presented.

CODE DESCRIPTION

Boiling water reactor inlet flow blockage analysis can be performed using the digital computer code MAYU-4b, which is a modified version of MAYU-4. This code analyzes one-dimensional thermal-hydraulic transients in rod bundles using a method-of-characteristics algorithm. The drift-flux model is employed, thus allowing for both co-current and countercurrent flow in a channel.

The revised code (MAYU-4b) features numerous improvements over the original code (MAYU-4). For the postdryout (PDO) heat transfer regime, a nonequilibrium vapor generation model and a detailed radiation heat transfer model have been added. In addition, the convective heat transfer in the PDO regime is now based on the superheated vapor temperature rather than saturation temperature. An improved critical quality/boiling length correlation was added to improve calculation of boiling transition. A drift-flux model was included that can predict CCFL conditions within the rod bundle. For elevated cladding temperatures ($>1800°F$), the user has the option of calculating the additional heat generation due to the exothermic zircaloy/water reaction. The maximum number of axial nodes has been increased to 100 and the code now has the ability to accommodate flow area changes, including grid spacers. Details of MAYU-4 are given in Reference 1, and the additional inputs required for MAYU-4b are listed in Appendix A.

Conservation Equations

The assumptions used in the derivation of the conservation equations are:

1. Subcooled boiling can be neglected
2. Kinetic and potential energy terms can be neglected in the mixture energy equation
3. Flow reversal does not take place
4. The flow is one-dimensional
5. Phasic slip is well quantified by a drift-flux model
6. Axial pressure effects on thermodynamic parameters can be ignored.

The resulting drift-flux conservation equations are presented below; their derivations are given in Appendix B.

Mixture Continuity Equation

$$\frac{\partial \langle j \rangle}{\partial z} = \left(\frac{1}{\rho_v} - \frac{1}{\rho_f}\right) \langle \Gamma \rangle - \frac{(1-\langle \alpha \rangle)}{\rho_f} \frac{\partial \rho_f}{\partial t} - \frac{\langle \alpha \rangle}{\rho_v} \frac{\partial \rho_v}{\partial t}$$

$$- \frac{\langle j_g \rangle}{\rho_v} \frac{\partial \rho_v}{\partial z} - \frac{\langle j \rangle}{A_{xs}} \frac{\partial A_{xs}}{\partial z} - \frac{1}{A_{xs}} \frac{\partial A_{xs}}{\partial t} . \qquad (1)$$

Vapor Continuity Equation

$$\frac{D_k \langle \alpha \rangle}{Dt} = \frac{\langle \Gamma \rangle}{\rho_v} - \frac{\langle \alpha \rangle}{\rho_v} \frac{\partial \rho_v}{\partial t} - \langle j_g \rangle \frac{\langle \alpha \rangle}{\rho_v} \frac{\partial \rho_v}{\partial z}$$

$$- \langle\alpha\rangle \left[\frac{C_o + \rho_f \left(\langle j \rangle \frac{\partial C_o}{\partial G} + \frac{\partial V_{gj}}{\partial G} \right)}{1 + \rho_f \Delta\rho \langle\alpha\rangle \left(\langle j \rangle \frac{\partial C_o}{\partial G} + \frac{\partial V_{gj}}{\partial G} \right)} \right] \frac{\partial \langle j \rangle}{\partial z}$$

$$- \frac{\langle j_g \rangle}{A_{xs}} \frac{\partial A_{xs}}{\partial z} - \frac{\langle\alpha\rangle}{A_{xs}} \frac{\partial A_{xs}}{\partial t} \qquad (2)$$

where

$$\frac{D_k \langle\alpha\rangle}{Dt} = \frac{\partial \langle\alpha\rangle}{\partial t} + C_k \frac{\partial \langle\alpha\rangle}{\partial z}$$

$$\Delta\rho \overset{\Delta}{=} \rho_f - \rho_v$$

$$\langle j_g \rangle = \langle\alpha\rangle \left(C_o \langle j \rangle + V_{gj} \right)$$

and the kinematic wave velocity, C_k, is given by

$$C_k = \frac{C_o \langle j \rangle + V_{gj} + \langle\alpha\rangle \left[\langle j \rangle \frac{\partial C_o}{\partial \langle\alpha\rangle} + \frac{\partial V_{gj}}{\partial \langle\alpha\rangle} \right]}{1 + \Delta\rho \langle\alpha\rangle \left(\langle j \rangle \frac{\partial C_o}{\partial G} + \frac{\partial V_{gj}}{\partial G} \right)} \quad .$$

Mixture Energy Equation

$$(h_v - h_\ell) \langle \Gamma \rangle = \left[\frac{q'' P_H}{A_{xs}} + \frac{1}{J} \frac{\partial p}{\partial t} \right] - \rho_v \langle\alpha\rangle \frac{D_v h_v}{Dt}$$

$$- \rho_f (1 - \langle\alpha\rangle) \frac{D_\ell h_\ell}{Dt} \qquad (3)$$

where, phase-k,

$$\frac{D_k}{Dt} (\quad) = \frac{\partial}{\partial t} (\quad) + \langle u_k \rangle_k \frac{\partial}{\partial z} (\quad) \quad .$$

It should be noted that for the PDO heat transfer regime, an energy balance gives the total heat flux to the two-phase mixture as

$$q'' = q''_{conv} + (q''_\ell)_{rad} + (q''_v)_{rad} - (q''_{v\text{-}w})_{conv}$$

where $(q''_{v,w})_{conv}$ is the convective heat flux from the superheated vapor to the channel box (assumed to be at saturation temperature).

Single-Phase Conservation Equations. In the single-phase region, the energy equation reduces to

$$\frac{D_i h}{Dt} = \frac{1}{\rho_i}\left[\frac{q'' P_H}{A_{xs}} + \frac{1}{J}\frac{\partial p}{\partial t}\right] \tag{4}$$

and the continuity equation to

$$\frac{\partial \langle j \rangle}{\partial z} = -\frac{1}{\rho_i}\frac{D_i \rho_i}{Dt} - \frac{\langle j \rangle}{A_{xs}}\frac{\partial A_{xs}}{\partial z} - \frac{1}{A_{xs}}\frac{\partial A_{xs}}{\partial t} \tag{5}$$

where the subscript "i" denotes that the parameters are evaluated at the inlet to the heated channel.

Drift-Flux Parameters

The MAYU-4b code allows the user to choose from three drift-flux models. First, the user may input constant values for C_o and V_{gj}. Another option is the so-called ramp model, contained in the original version of MAYU,[1]

$$C_o = \begin{cases} a & , \langle\alpha\rangle < b \\ 1 + \left[\frac{a-1}{1-b}\right](1-\langle\alpha\rangle) & , \langle\alpha\rangle \geq b \end{cases} \tag{6a}$$

$$V_{gj} = \begin{cases} c\left[\frac{g g_c \sigma (\rho_f - \rho_g)}{\rho_f^2}\right]^{1/4} & , \langle\alpha\rangle < b \\ c\left[\frac{g g_c \sigma (\rho_f - \rho_g)}{\rho_f^2}\right]^{1/4} \frac{(1-\langle\alpha\rangle)}{1-b} & , \langle\alpha\rangle \geq b \end{cases} \tag{6b}$$

where a, b, and c are user inputs (preset to 1.13, 0.65, and 2.9, respectively). Finally, the user may choose the model developed by Ohkawa and Lahey.[2] This model automatically predicts CCFL conditions, if they exist, within the rod bundle. The drift-flux parameters used in this model are:

$$V_{gj} = V_{gj_1}$$

$$C_o = C_{o_1} \quad , \langle\alpha\rangle < d \tag{7a}$$

and,

$$V_{gj} = \min\left(V_{gj_1}, V_{gj_2}\right)$$

$$C_o = \min\left(C_{o_1}, C_{o_2}\right) \quad , \langle\alpha\rangle \geq d \tag{7b}$$

where

$$V_{gj_1} \triangleq 2.9 \left[\frac{g g_c \sigma (\rho_f - \rho_g)}{\rho_f^2}\right]^{1/4} \tag{7c}$$

$$V_{gj_2} \triangleq Y \left[\frac{g g_c \sigma (\rho_f - \rho_g)}{\rho_f^2}\right]^{1/4} \left[1 - \left(\frac{\langle\alpha\rangle - d}{1-d}\right)^2\right] \tag{7d}$$

$$C_{o_1} \triangleq \left[1.2 - 0.2 \left(\frac{\rho_g}{\rho_f}\right)^{1/2}\right] \left[1 - \exp\left(-18 \langle\alpha\rangle\right)\right] \tag{7e}$$

$$C_{o_2} \triangleq 1.0 + 0.2 \left[1 - \left(\frac{\rho_g}{\rho_f}\right)^{1/2}\right] \left[1 - \left(\frac{\langle\alpha\rangle - d}{1-d}\right)^2\right] \tag{7f}$$

and

$$d \triangleq 0.5881164 - 1.81701 \left(\frac{\rho_g}{\rho_f}\right)^{1/2} + 2.00025 \left(\frac{\rho_g}{\rho_f}\right) - 3.34398 \left(\frac{\rho_g}{\rho_f}\right)^{3/2} \tag{7g}$$

$$Y \triangleq \max\left(3.136, Y_1\right) \tag{7h}$$

$$\begin{aligned} Y_1 \triangleq\ & 4.72085 - 17.26736 \left(\frac{\rho_g}{\rho_f}\right)^{1/2} + 56.14883 \left(\frac{\rho_g}{\rho_f}\right) \\ & + 113.21605 \left(\frac{\rho_g}{\rho_f}\right)^{3/2} - 1250.603 \left(\frac{\rho_g}{\rho_f}\right)^2 \\ & + 3039.7669 \left(\frac{\rho_g}{\rho_f}\right)^{5/2} - 2431.8228 \left(\frac{\rho_g}{\rho_f}\right)^3 . \end{aligned} \tag{7i}$$

The drift-flux parameters used in the Ohkawa-Lahey model are shown in Figures 1 and 2 for 1000 and 100 psia. The trends are consistent with the existing data. The (CCFL) flooding curves that result from the Okhawa-Lahey model are compared with Kutateladze's CCFL correlation in Figure 3. The agreement is excellent at 1000 psia, the pressure of interest, and quite good even at 100 psia. For comparison, the flooding curve predicted by the ramp model[1] is shown in Figure 4 for 1000 psia. This plot was constructed using the preset values of a, b, and c in MAYU-4.[1] It is obvious that the Ohkawa-Lahey model offers a significant improvement over the ramp model.

One-Dimensional Radial Heat Conduction Model

To obtain the temperature distribution in the fuel rods, the following (conduction) equation must be solved:

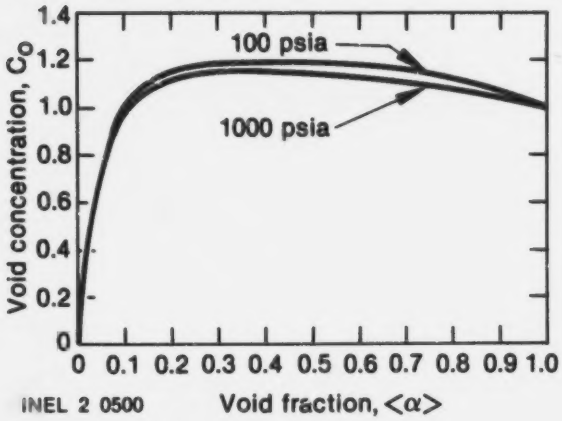

Figure 1. Void concentration parameter versus void fraction—Ohkawa-Lahey model.

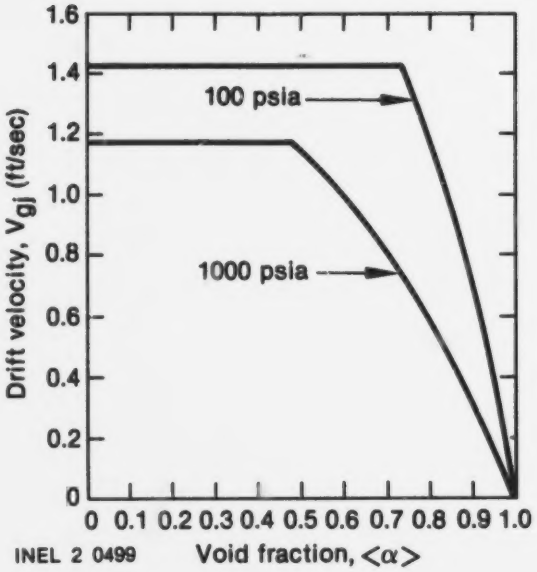

Figure 2. Drift velocity versus void fraction—Ohkawa-Lahey model.

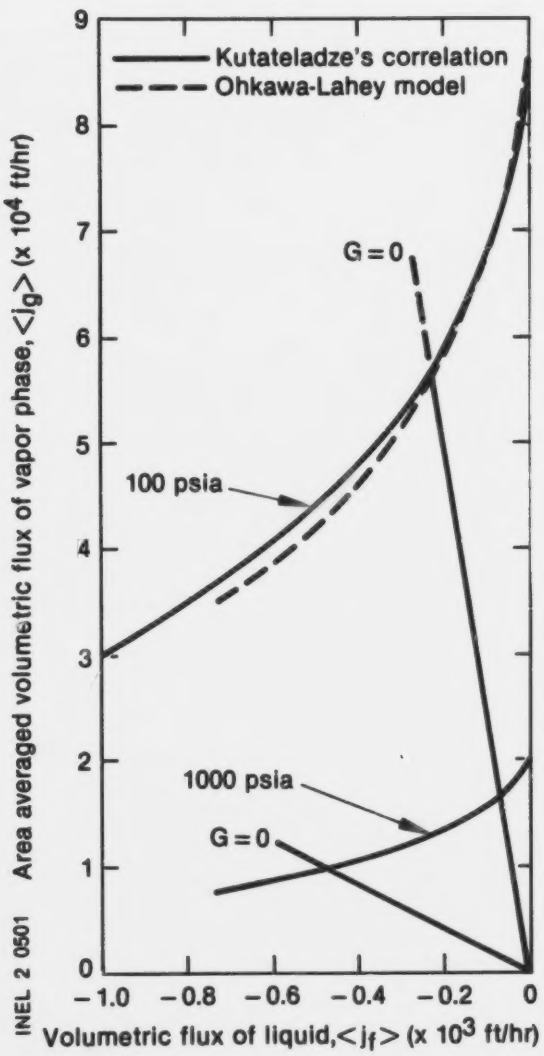
Kutateladze's correlation
Ohkawa-Lahey model
G = 0
100 psia
1000 psia
G = 0
Area averaged volumetric flux of vapor phase, <j_g> (x 10^4 ft/hr)
−1.0 −0.8 −0.6 −0.4 −0.2 0
Volumetric flux of liquid, <j_f> (x 10^3 ft/hr)
INEL 2 0501

Figure 3. Kutateladze's correlation and flooding curves predicted by the Ohkawa-Lahey model.

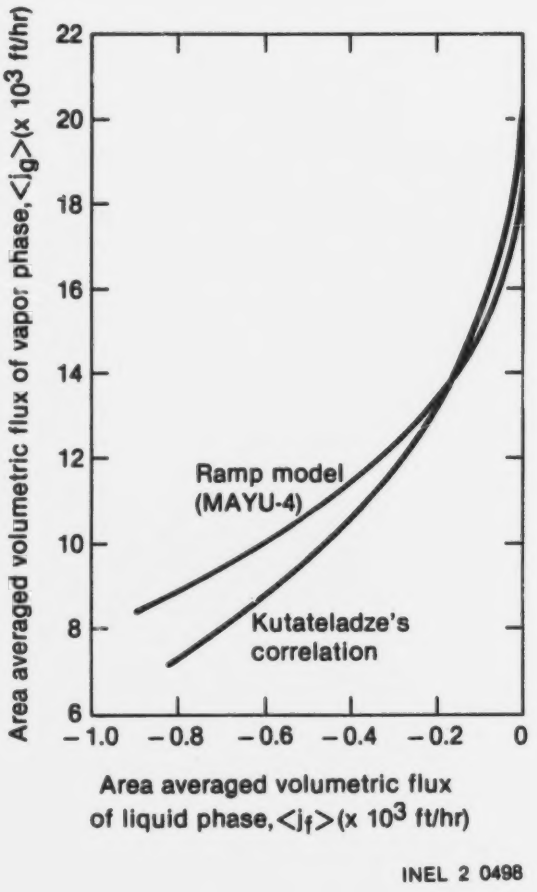

Figure 4. Kutateladze's correlation and flooding curve predicted by the ramp model.

$$\rho c_p \frac{\partial T}{\partial t} = \nabla \cdot \kappa \nabla T + q''' \quad . \tag{8}$$

By assuming angular symmetry and neglecting axial effects, we obtain in cylindrical coordinates,

$$\rho c_p \frac{\partial T}{\partial t} = \frac{1}{r} \frac{\partial}{\partial r} \left(r \kappa \frac{\partial T}{\partial r} \right) + q''' \quad . \tag{9}$$

This equation is finite differenced and numerically evaluated, subject to the following boundary conditions:

$$-\kappa \left. \frac{\partial T}{\partial r} \right|_{r=r_n} = q'' (r_n, t) = H_\infty [T_n(t) - T_\infty(t)] + q_R'' \tag{10a}$$

$$-\kappa \left. \frac{\partial T}{\partial r} \right|_{r=r_m} = q'' (r_m, t) = H_{gap} [T_{m-1}(t) - T_m(t)] \tag{10b}$$

$$-\kappa \left. \frac{\partial T}{\partial r} \right|_{r=r_{m-1}} = q'' (r_{m-1}, t) = \left(\frac{r_m}{r_{m-1}} \right) q'' (r_m, t) \tag{10c}$$

$$\left. \frac{\partial T}{\partial r} \right|_{r=0} = 0 \quad . \tag{10d}$$

where q_R'' is the heat flux due to radiation heat transfer.

MAYU-4b uses the same Crank-Nicolson formulation as MAYU-4; however, the boundary condition at the outer cladding surface now includes a radiative heat flux term (q_R''). The revised code also has the ability to calculate the additional heat generation ($q'''_{Zr\text{-}H_2O}$) due to the exothermic zircaloy-water reaction, which becomes appreciable for cladding temperatures above about 1800°F.

The resulting system of equations can be conveniently expressed in matrix form as[3]

$$D_k (\underline{T}' - \underline{T}) = L_k (\underline{T}' + \underline{T}) + \underline{Q}_k \tag{11}$$

where, for time step-k,

$$\underline{T} \overset{\Delta}{=} (T_{1,k}, T_{2,k}, \ldots, T_{n,k})^T \tag{12a}$$

$$\underline{T}' \overset{\Delta}{=} (T_{1,k+1}, T_{2,k+1}, \ldots, T_{n,k+1})^T \tag{12b}$$

$$D_k \overset{\Delta}{=} \frac{1}{2} [(\rho c_p)_{i,k} + (\rho c_p)_{i,k+1}] \delta_{ij} \tag{12c}$$

$$\underline{Q}_k \overset{\Delta}{=} \frac{\Delta t}{2} [q'''_{1,k} + q'''_{1,k+1}, \ldots, q'''_{n-1,k} + q'''_{n-1,k+1},$$

$$q'''_{n,k} + q'''_{n,k+1} + \frac{2}{(r_n - r_{n-1})} (H_{\infty,k} T_{\infty,k} + H_{\infty,k+1} T_{\infty,k+1})$$

$$- \frac{4}{(r_n - r_{n-1})} q''_{R,k}] \qquad (12d)$$

$$\underline{L}_k \triangleq \ell_{i,k}^{(D-1)} \delta_{ij+1} + \ell_{i,k}^{(D)} \delta_{ij} + \ell_{i,k}^{(D+1)} \delta_{ij-1} \; . \qquad (12e)$$

The elements $\ell_{i,k}$ of the tridiagonal matrix, L_k, are given in Table 1.

Table 1. Elements of matrix L_k

Centerline Node (i = 1)	$\ell_{1,k}^{(D)} \triangleq - \frac{2\Delta t \kappa_{1,k}}{(r_2)^2}$
	$\ell_{1,k}^{(D+1)} \triangleq - \ell_{1,k}^{(D)}$
Interior Nodes ($2 \leq i \leq m-2$, $m+1 \leq i \leq n-1$)	$\ell_{i,k}^{(D-1)} \triangleq \frac{\Delta t}{2} \left(1 + \frac{r_{i-1}}{r_i}\right) \frac{\kappa_{i-1/2,k}}{(r_{i+1} - r_{i-1})(r_i - r_{i-1})}$
	$\ell_{i,k}^{(D+1)} \triangleq \frac{\Delta t}{2} \left(1 + \frac{r_{i+1}}{r_i}\right) \frac{\kappa_{i+1/2,k}}{(r_{i+1} - r_{i-1})(r_{i+1} - r_i)}$
	$\ell_{i,k}^{(D)} \triangleq - \left[\ell_{i,k}^{(D-1)} + \ell_{i,k}^{(D+1)}\right]$
Fuel Pellet Surface Node (i = m - 1)	$\ell_{m-1,k}^{(D-1)} \triangleq \frac{\Delta t}{2} \left(1 + \frac{r_{m-2}}{r_{m-1}}\right) \frac{\kappa_{m-3/2,k}}{(r_{m-1} - r_{m-2})^2}$
	$\ell_{m-1,k}^{(D+1)} \triangleq \frac{\Delta t}{2} \left(\frac{r_m}{r_{m-1}}\right) \frac{2H_{gap,k}}{(r_{m-1} - r_{m-2})}$
	$\ell_{m-1,k}^{(D)} \triangleq - \left[\ell_{m-1,k}^{(D-1)} + \ell_{m-1,k}^{(D+1)}\right]$
Inner Cladding Surface Node (i = m)	$\ell_{m,k}^{(D+1)} \triangleq \frac{\Delta t}{2} \frac{2H_{gap,k}}{(r_{m+1} - r_m)}$

MICROFILMED FROM BEST AVAILABLE COPY

Table 1. (continued)

$$\ell_{m,k}^{(D+1)} \triangleq \frac{\Delta t}{2}\left(\frac{r_m}{r_{m-1}}\right)\frac{2H_{gap,k}}{(r_{m-1} - r_{m-2})}$$

$$\ell_{m,k}^{(D)} \triangleq -\left[\ell_{m,k}^{(D-1)} + \ell_{m,k}^{(D+1)}\right]$$

Outer Cladding Surface Node (i = n)

$$\ell_{n,k}^{(D-1)} \triangleq \frac{\Delta t}{2}\left(1 + \frac{r_{n-1}}{r_n}\right)\frac{\kappa_{n-1/2,k}}{(r_n - r_{n-1})^2}$$

$$\ell_{n,k}^{(D)} \triangleq -\left[\ell_{n,k}^{(D-1)} + \frac{\Delta t}{2}\frac{H_{\infty,k} + H_{\infty,k+1}}{(r_n - r_{n-1})}\right]$$

Metal-Water Reaction Model

If the zircaloy cladding temperature exceeds about 1800°F, an exothermic reaction occurs,

$$Zr + 2H_2O \rightarrow ZrO_2 + 2H_2 + \Delta \tag{13}$$

where Δ is the energy generated by this reaction. This reaction is initially controlled by the gaseous diffusion of water vapor through the hydrogen boundary layer. Later, as the cladding oxidizes, the controlling mechanism becomes the solid-state diffusion of oxygen into the ZrO_2. Both processes have been investigated by Baker and Just.[4] They found that the rate at which the thickness of the oxidized layer increases is given by

$$\dot{x}_1 = \frac{(1.849E\text{-}7)RP\ (TFILM)^{0.68}}{(RP\text{-}XO/30.48)^{2.0}} \tag{14a}$$

when gaseous diffusion controls, and by

$$\dot{x}_2 = \frac{0.394}{XO}\exp\left(-\frac{41220}{ROD+460}\right) \tag{14b}$$

when the reaction is limited by solid-state diffusion. The variables used are defined as,

$\dot{x}_{1,2}$	=	growth rate of oxidized layer (cm/s)
RP	=	fuel rod radius (ft)
XO	=	oxidized layer thickness (cm)
TFILM	=	arithmetic average of cladding temperature and steam temperature (K)
ROD	=	cladding temperature (°F).

MAYU-4b currently assumes that the cladding is not breached and calculates the oxidized layer thickness on the outside of the cladding as

$$XO_{k+1} = XO_k + \dot{x}\,\Delta t \tag{15}$$

$$\dot{x} = \min\,(\dot{x}_1, \dot{x}_2)\ . \tag{16}$$

The rate of zirconium reaction per unit volume is given by

$$\dot{Zr} = \frac{(\pi D \dot{x} L)}{(\pi \frac{D^2}{4} L)} = 4\,\frac{\dot{x}}{D} \tag{17}$$

where "D" is the fuel rod diameter (i.e., cladding outside diameter) in centimeters. For 140,000 calories of heat release per gram-mole of zirconium oxidized, the resulting volumetric heat release is

$$q'''_{m-w} = 5.3058E8\,\frac{\dot{x}}{D} \qquad \text{(Btu/hr-ft}^3\text{ of fuel rod)} \tag{18}$$

If the reacting interface is located in node-i of the cladding, the corresponding volumetric heat release for node-i is given by,

$$(q'''_i)_{Zr\text{-}H_2O} = (q'''_{m-w})\,\frac{\pi\frac{D^2}{4}L}{\pi D \Delta R_i L} = 1.38645E8\,\frac{\dot{x}}{\Delta R_i} \qquad \text{(Btu/hr-ft}^3\text{ of cladding)} \tag{19}$$

where ΔR_i is the thickness (in cm) of node-i.

Although the Baker-Just model is currently used in MAYU-4b, other similar models could be readily incorporated if improved accuracy were desired. Moreover, a rod swell and burst criterion might be considered in future investigations, so that the zircaloy-water reaction could take place on the interior surface of the breached cladding.

Thermal Limits Correlations

Co-Current Flow. MAYU-4b allows the user to choose from two critical quality-boiling length correlations for co-current flow. The user may select the form used in MAYU-4,[1]

$$x_c = \frac{1}{R_F}\,\frac{aL_B}{(b+L_B)} \tag{20}$$

where

L_B = boiling length

R_F = user-supplied correlation factor for each rod group quantifying the effect of the rod power peaking patterns

a,b = user-supplied correlated coefficients (preset to 0.553 and 55.21, respectively).

The user may also select the so-called CISE-Lahey correlation,

$$x_c = \left(\frac{1.24}{F_L}\right)^{1/2} \frac{AL_B}{(B+L_B)} \tag{21}$$

where

$$A \triangleq 1.055 - 0.013 \left(\frac{p-600}{400}\right)^2 - 1.233 \left(\frac{G}{10^6}\right) + 0.907 \left(\frac{G}{10^6}\right)^2 - 0.285 \left(\frac{G}{10^6}\right)^3$$

$$B \triangleq 17.980 + 78.873 \left(\frac{G}{10^6}\right) - 35.474 \left(\frac{G}{10^6}\right)^2$$

F_L = local peaking factor for each rod group

G = mass flux (lb/hr-ft^2)

p = pressure (psia).

The latter correlation, Equation (21), is the recommended choice for the analysis of BWRs.

Countercurrent Flow. The so-called Walkus-Griffith model for boiling transition in countercurrent flow is given by[3]

$$\frac{q_c''(z)}{q''_{max}} = 0.9 \quad , \quad 0 \leq \langle\alpha\rangle \leq 0.20 \tag{22a}$$

$$\frac{q_c''(z)}{q''_{max}} = 1.125\,[1-\langle\alpha(z)\rangle], \quad 0.20 \leq \langle\alpha\rangle \leq 1.0 \tag{22b}$$

where the limiting heat flux, q''_{max}, is defined as

$$q''_{max} = 0.131\, h_{fg} \left[\rho_g \left(1 + \frac{\rho_g}{\rho_f}\right)\right]^{1/2} \left[\sigma\, gg_c\, (\rho_f-\rho_g)\right]^{1/4} \tag{23}$$

Heat Transfer Correlations

The criteria used for selecting the correct heat transfer regime is shown in Table 2, along with the corresponding correlations. These correlations are defined as follows:

Table 2. Heat transfer correlations

Criteria	Heat Transfer Regime	Model Used
$X_e < 0$	Single-phase liquid	Dittus-Boelter
$T_\infty < T_{\ell b}$		
$x_e < 0$	Single-phase liquid; subcooled boiling	Jens-Lottes
$T_{\ell b} < T \leq T_f$		
$x_e < x_c$; $j_f > 0$	Co-current two-phase nucleate boiling	Jens-Lottes
$T_w - T_\infty < \Delta T_{rewet}$		
$x_e < x_c$; $j_f > 0$	Co-current two-phase film boiling	Max (modified Dittus-Boelter, Bromley)
$T_w - T_\infty \geq \Delta T_{rewet}$		
$x_c \leq x_e < 1$	Co-current two-phase film boiling	Max (modified Dittus-Boelter, Bromley)
$j_f > 0$		
$\langle x \rangle = 1$	Single-phase vapor	Modified Dittus-Boelter
$j_f < 0$; $q''(Z) < q_c''(Z)$	Countercurrent two-phase nucleate boiling	Jens-Lottes
$T_w - T_\infty < \Delta T_{rewet}$		
$j_f < 0$; $q''(Z) < q_c''(Z)$	Countercurrent two-phase film boiling	Bromley
$T_w - T_\infty \geq \Delta T_{rewet}$		
$j < 0$; $q''(Z) \geq q_c''(Z)$	Countercurrent two-phase film boiling	Bromley

where

$T_{\ell b} \triangleq$ bulk fluid temperature at point of (subcooled) boiling initiation.

REPRODUCED FROM BEST AVAILABLE COPY

Dittus-Boelter

$$H_{\infty} = 0.023\ (Re_{\ell})^{0.8}\ (Pr_{\ell})^{0.4}\ (\frac{\kappa_{\ell}}{D_H})\ . \tag{24}$$

Jens-Lottes

$$H_{\infty} = \frac{q''}{\Delta T_{J-L}} \tag{25}$$

where

$$\Delta T_{J-L} = T_w - T_f = 60\ \exp\ (-\frac{p}{600})\ (\frac{q''}{10^6})^{1/4}\ . \tag{26}$$

Modified Dittus-Boelter

$$H_{\infty} = 0.023\ (\frac{G_v D_H}{\mu_v})^{0.8} (Pr_v)^{0.4} \sqrt{\frac{(T_v+460)}{(T_w+460)}}\ (\frac{\kappa_v}{D_H}) \tag{27a}$$

where

$$G_v = G\langle\alpha\rangle\ . \tag{27b}$$

Bromley

$$H_{\infty} = 0.62\ [\frac{k_g^3\ \rho_g(\rho_f-\rho_g)h_{fg}\ g}{\mu_g(T_w-T_f)\ L_T}]^{1/4} \tag{28}$$

where L_T is the Taylor instability wavelength and is given by

$$L_T = 2\pi\ [\frac{g_c\sigma}{g(\rho_f-\rho_g)}]^{1/2}\ . \tag{29}$$

As the mass flux approaches zero, the modified Dittus-Boelter equation is no longer valid. Since the Bromley correlation is based on pool boiling data, the heat transfer coefficient in the co-current two-phase film boiling regime is given by

$$H_{\infty} = \text{Max (modified Dittus-Boelter, Bromley)}\ . \tag{30}$$

Note that the convective heat transfer in the film boiling regime is based on the actual temperature difference, $(T_w - T_v)$, rather than $(T_w - T_{sat})$, as in MAYU-4.[1]

NONEQUILIBRIUM VAPOR GENERATION

Vapor generation in the postdryout heat transfer regime is normally bracketed by two models. The so-called "frozen droplet" model assumes that, subsequent to boiling transition, no further liquid droplet evaporation occurs. This assumption results in all of the heat transfer going to vapor superheat. The other possibility is that of thermal equilibrium, in which all of the heat transfer is assumed to go to vapor formation. The MAYU-4 code assumed thermal equilibrium.

Figures 5 and 6 compare the trends of surface temperature, flow quality, and volumetric vapor generation rate with the results predicted by each of these models. Obviously, a more mechanistic model is required for realistic analyses.

A better approach would be to consider a two-step heat transfer model. In this model it is assumed that, subsequent to boiling transition, the vapor temperature rises as it becomes superheated. The heat is then transferred from the superheated vapor to the saturated liquid droplets, resulting in droplet evaporation. Saha[5] has developed a postdryout (PDO) heat transfer model that is based on these ideas and on experimental data in the dispersed droplet flow regime. This model permits a more accurate calculation of fluid conditions than either the thermal equilibrium or "frozen droplet" models; hence, in principle, allowing a more accurate prediction of PDO heat transfer.

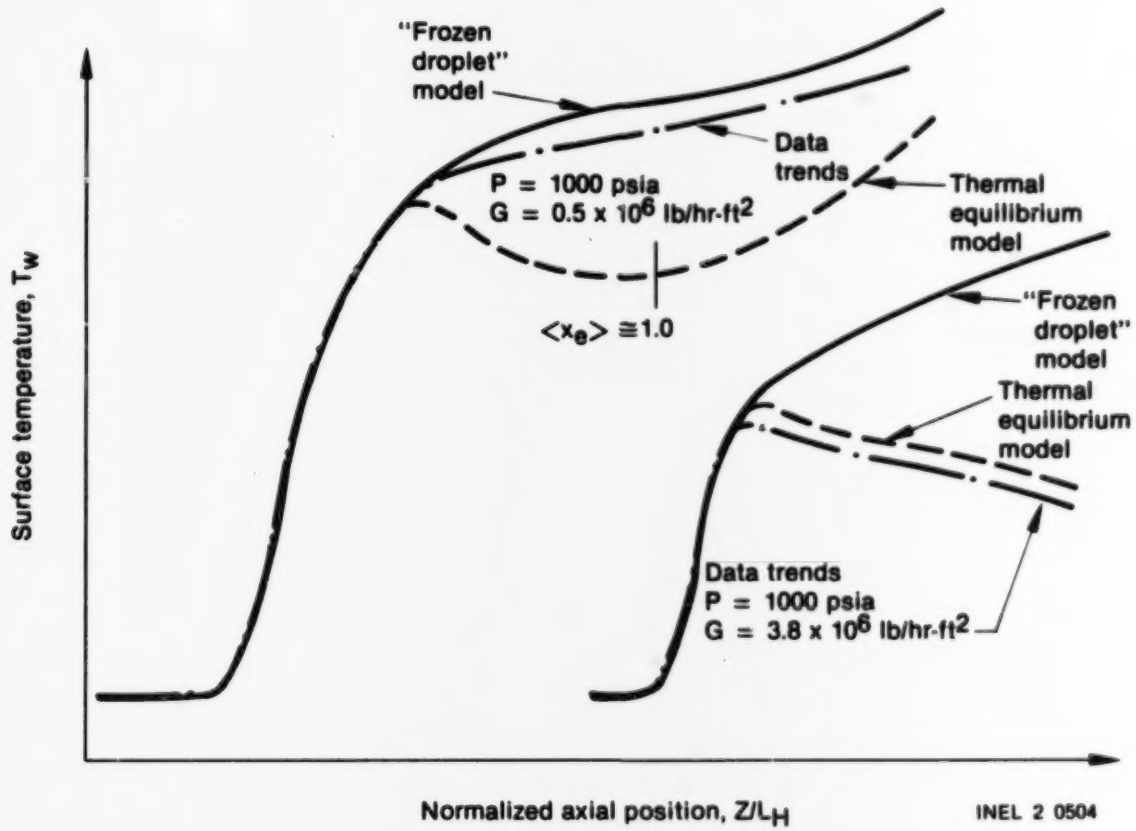

Figure 5. Typical high-quality PDO heat transfer data trends[6].

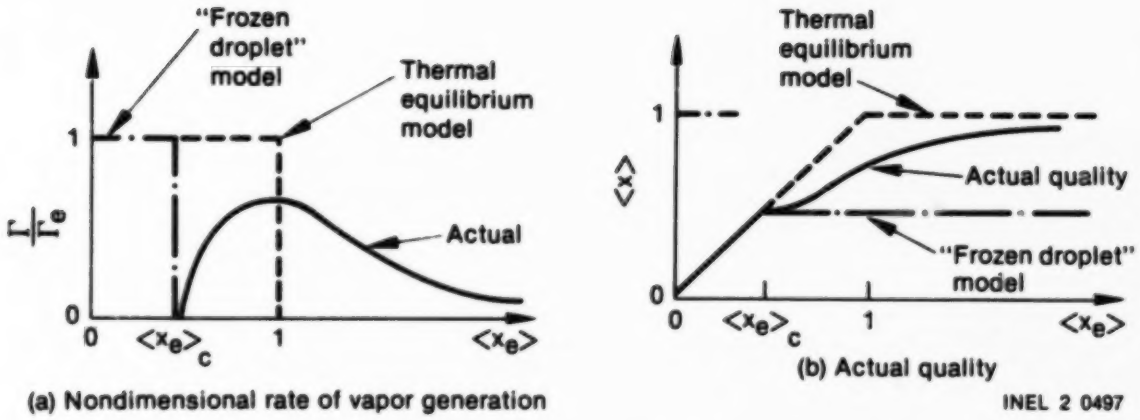

Figure 6. Comparison of the thermal equilibrium model and the "frozen droplet" model with typical data trends.

Nonequilibrium Vapor Generation Model

Saha[5] assumes no heat transfer directly from the wall to the droplets, and obtains the following expression for conservation of energy for the liquid phase:

$$\Gamma_{v\text{-}d} = \frac{q''_{v\text{-}d} P_H}{A_{xs}\, h_{fg}} \quad . \tag{31}$$

Assuming all droplets are of the same size, the heat transfer from the vapor to the liquid is then given by

$$q''_{v\text{-}d}\, P_H\, \Delta Z = N_d\, A_{xs}\, \Delta Z\, (\pi\delta^2)\, H_{v\text{-}d}\, (T_v - T_{sat}) \tag{32}$$

where $(\pi\delta^2)$ is the surface area of a droplet of diameter δ. For droplets of uniform size, the number density is given by

$$N_d = \frac{(1-\langle\alpha\rangle)}{\pi \frac{\delta^3}{6}} \quad . \tag{33}$$

Combining these equations yields a volumetric vapor generation rate given by

$$\Gamma_{v\text{-}d} = 6(1-\langle\alpha\rangle)\, \frac{H_{v\text{-}d}}{\delta h_{fg}}\, (T_v - T_{sat}) \quad . \tag{34}$$

Drake[5] has developed an expression for the heat transfer coefficient between vapor and a sphere. Assuming this expression holds for the droplets,

$$H_{v\text{-}d} = \frac{K_v}{\delta} \left[2 + 0.459 \left\{\frac{\rho_v (u_v - u_\ell)\delta}{\mu_v}\right\}^{0.55} (Pr_v)^{1/3}\right] \quad . \tag{35}$$

Defining,

$$K_1 \triangleq 6[2 + 0.459 \left\{\frac{\rho_v(u_v-u_\ell)\delta}{\mu_v}\right\}^{0.55} (Pr_v)^{1/3}] \left(\frac{D_H}{\delta}\right)^2 \tag{36}$$

the volumetric vapor generation rate in Equation (34) becomes

$$\Gamma_{v-d} = \frac{K_1 K_v (1-\langle\alpha\rangle)}{D_H^2 h_{fg}} (T_v - T_{sat}) \ . \tag{37}$$

Saha developed an expression for the droplet diameter by performing a mass balance on the liquid phase at the dryout location and any point downstream:

$$\rho_f j_{f,DO} = G (1-\langle x\rangle_{DO}) = \dot{N}_{d,DO} \rho_f \frac{\pi}{6} \delta_{DO}^3 \tag{38a}$$

$$\rho_f j_f = G(1-\langle x\rangle) = \dot{N}_d \rho_f \frac{\pi}{6} \delta^3 \tag{38b}$$

where $\dot{N}_d$ is defined as the droplets per unit volume, per unit time at a given location downstream of the dryout point. However, Saha's analysis[5] considered co-current flow situations. Let us assume that the liquid droplets are carried along by the vapor. This assumption is obviously good for high (co-current) flow situations and is expected to be valid for countercurrent flows, in which case the liquid film drains down the channel wall while liquid droplets rise with the vapor within the bundle. Assuming the droplet and the vapor velocity are the same, a mass balance yields

$$\rho_f j_{f,DO} \simeq \rho_f (1-\langle\alpha\rangle_{DO}) u_{g,DO} = \dot{N}_{d,DO} \rho_f \frac{\pi}{6} \delta_{DO}^3 \tag{39a}$$

$$\rho_f j_f \simeq \rho_f (1-\langle\alpha\rangle) u_g = \dot{N}_d \rho_f \frac{\pi}{6} \delta^3 \ . \tag{39b}$$

Now, assuming no droplet breakup or coalescense (i.e., $\dot{N}_{d,DO} = \dot{N}_d$), we have

$$\frac{\delta}{\delta_{DO}} = \left(\frac{(1-\langle\alpha\rangle) u_g}{(1-\langle\alpha\rangle_{DO}) u_{g,DO}}\right)^{1/3} = \left(\frac{(1-\langle\alpha\rangle) j_g}{(1-\langle\alpha\rangle_{DO}) j_{g,DO}} \frac{\langle\alpha\rangle_{DO}}{\langle\alpha\rangle}\right)^{1/3} \ . \tag{40}$$

To find the droplet diameter at the dryout point, δ_{DO}, let us consider the entrainment process at that location. Near the dryout point, droplets are entrained from the wavy film at the wall into the vapor core. The droplet size is proportional to the height of the surface waves, which is proportional to the film thickness. The wave deformation is controlled by the balance of inertial and surface tension forces. The Weber number relates these forces as

$$W_e = \frac{\rho_v (u_g - u_{f\ell})^2 L_c}{\sigma g_c} \tag{41}$$

where

$u_{\ell\ell} \overset{\Delta}{=}$ area-averaged velocity of liquid film

$L_C \overset{\Delta}{=}$ some characteristic length.

Assuming that the liquid film velocity at the dryout point is negligible compared to the vapor velocity, and that the void fraction approaches unity, we can replace the relative velocity term with the superficial vapor velocity, j_g. Saha chose the characteristic length used by Ishii and Grolmes[7] in their inception criteria for entrainment,

$$L_c = \sqrt{\frac{\sigma g_c}{g(\rho_f - \rho_v)}} \quad . \tag{42}$$

Combining these equations and assumptions yields a dryout diameter in the following form,[5]

$$\frac{\delta_{DO}}{D_H} = C \left[\frac{\rho_v j_{g,DO}^2 \sqrt{\sigma g_c / g(\rho_f - \rho_v)}}{\sigma g_c}\right]^n \quad . \tag{43}$$

Saha determined the constants experimentally to be C = 1.47 and n = -0.675. Thus, combining Equations (43) and (40), we obtain

$$\frac{\delta}{D_H} = 1.47 \left[\frac{\rho_v j_{g,DO}^2 \sqrt{\sigma / g g_c (\rho_f - \rho_v)}}{\sigma}\right]^{-0.675} \left[\frac{(1-\langle\alpha\rangle) j_g^{\langle\alpha\rangle} D_O}{(1-\langle\alpha\rangle_{DO}) j_{g,DO}^{\langle\alpha\rangle}}\right]^{1/3} \quad . \tag{44}$$

In summary, the *modified* Saha model, used in MAYU-4b, is given by

$$\Gamma_{v-d} = \frac{K_1 K_v (1-\langle\alpha\rangle)}{D_H^2 \, h_{fg}} (T_v - T_{sat}) \tag{45}$$

where K_i is given by Equation (36) and $\frac{\delta}{D_H}$ is given by Equation (44).

Calculation of Superheated Vapor Enthalpy in the PDO Regime

The mixture energy balance, Equation (3), must be solved for the superheated vapor enthalpy, h_v, to determine the superheated vapor temperature, T_v. The vapor enthalpy is also used to calculate the change in vapor density with respect to distance ($\partial\rho_v/\partial z$). This term is needed to solve the mixture and vapor continuity equations [Equations (1) and (2)]. For the PDO regime, the total volumetric vapor generation rate is thus given by

$$\Gamma = \Gamma_p + \Gamma_{v-d} + \Gamma_{rad} \quad . \tag{46}$$

Since we desire the vapor enthalpy, the heat flux to the vapor must be used in the form

$$q_v'' = q'' - \frac{(q_\ell)_{rad}}{A_{HT}} \quad . \tag{47}$$

Model Verification

Verification of the nonequilibrium vapor generation model was made by comparing results predicted by the model with appropriate experimental data.[8,9] Figures 7, 8, and 9 show wall superheat ($T_w - T_{sat}$), versus the equilibrium quality, x_e, for three different experiments. These graphs compare the results from the equilibrium and nonequilibrium (modified Saha and modified Dittus-Boelter) models with the measured wall temperatures. In all three cases it can be seen that the nonequilibrium model predicts wall temperatures much more accurately than the thermal equilibrium model. As equilibrium quality increases, a pure (superheated) vapor state is approached (i.e., flow quality approaches unity). Under these conditions the predictions of both models should agree. This is evident in Figure 9, which corresponds to the experiment with the highest mass flux (i.e., the one closest to thermal equilibrium).

The results of the intermediate flow rate case were used to examine the trends in the volumetric vapor generation and flow quality calculations. Figure 10 is a plot of the predicted volumetric vapor generation rate versus axial position. Note the similarity to the expected trends presented in Figure 6(a). With a uniform axial heat flux profile, the vapor generation rate is constant throughout the nucleate boiling regime. At the dryout point the vapor generation drops to essentially zero. At this location the vapor temperature is still saturated, resulting in virtually no heat transfer to the liquid droplets. As the vapor superheat increases, the Γ increases to a peak, after which it decreases. This decrease is due to the reduced surface area for vapor-liquid heat transfer as the flow quality approaches unity.

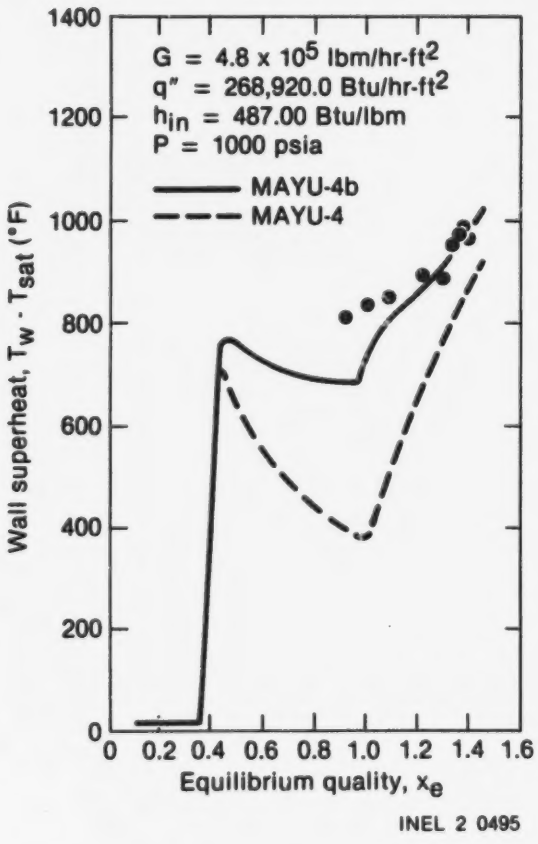

Figure 7. Comparison of MAYU-4b, MAYU-4, and experimental results[9].

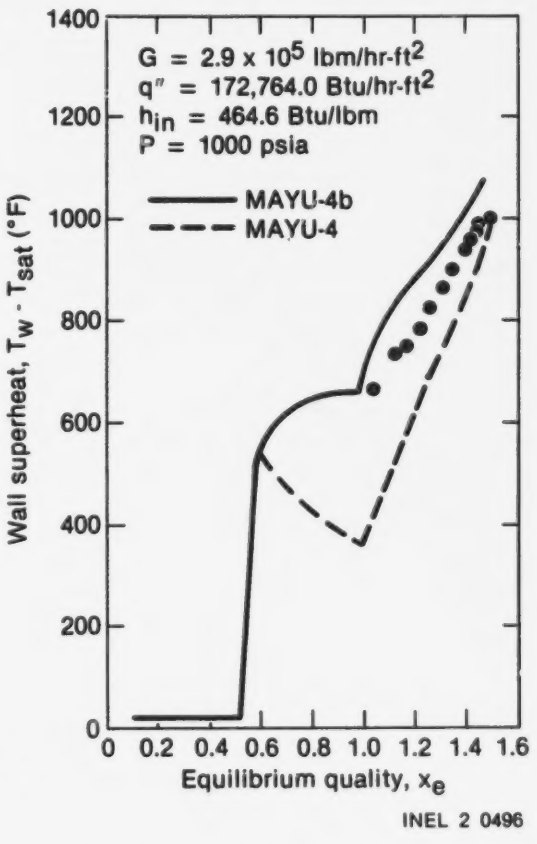

Figure 8. Comparison of MAYU-4b, MAYU-4, and experimental results[9].

Figure 11 shows the relation between the predicted flow quality and the thermodynamic equilibrium quality for the same case. Once again, the nonequilibrium model is seen to be in good agreement with the expected trends shown in Figure 6(b).

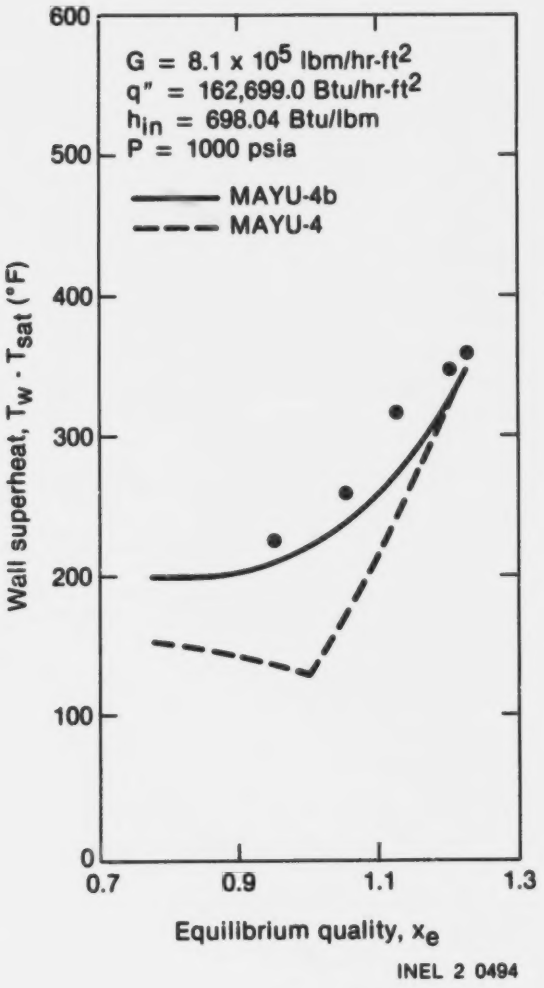

Figure 9. Comparison of MAYU-4b, MAYU-4, and experimental results[9].

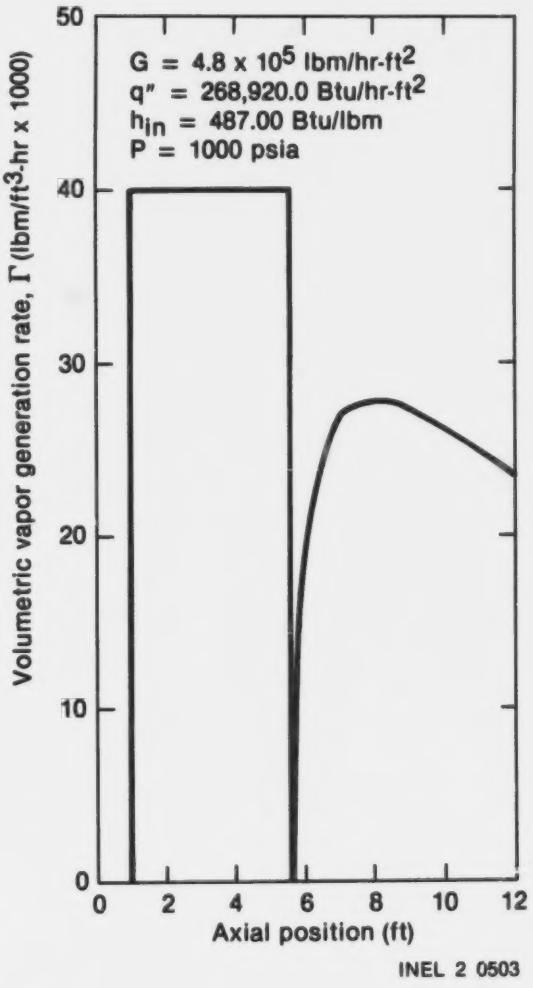

Figure 10. Typical trend of volumetric vapor generation rate predicted by MAYU-4b as a function of axial position.

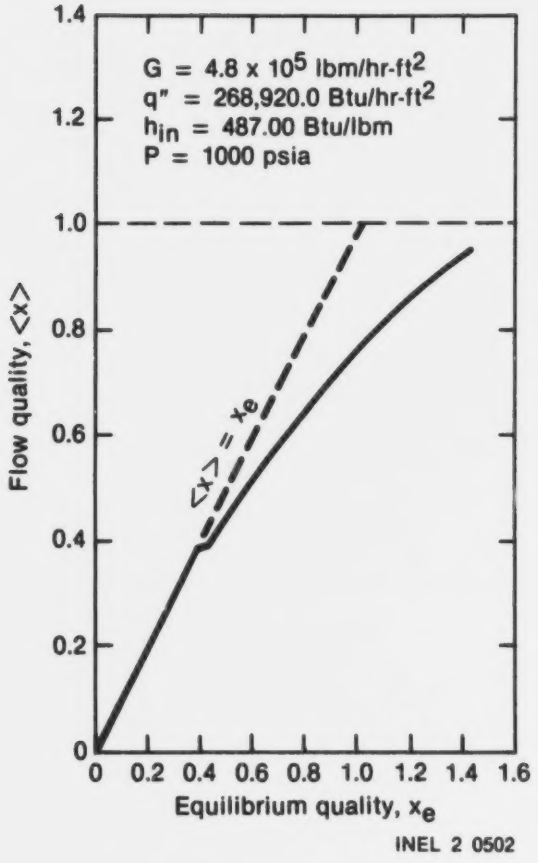

Figure 11. Typical trend of flow quality predicted by MAYU-4b as a function of equilibrium quality.

RADIATIVE HEAT TRANSFER

Radiative heat transfer models for light water reactor accident analysis have been presented by numerous authors. For a single-channel analysis, we require a model that has the capability to calculate surface-to-surface radiative heat transfer and radiative heat transfer to the vapor and liquid droplets. Mandell[10] has written such a model for the TRAC code, and the model was adapted to the MAYU-4b code.

Radiative Heat Transfer Model

The assumptions made in the derivation of this model[10] include:

1. The surfaces are gray and diffuse (i.e., emission and reflection are independent of wavelength)
2. The channel wall can be considered to be one surface at a uniform temperature
3. Each rod is one surface at a uniform temperature
4. Radiative heat transfer in the axial direction is negligible
5. The fluid is gray (i.e., the vapor and liquid absorption coefficients are independent of wavelength)
6. The steam temperature at any axial position is constant
7. The water droplet temperature at any axial position is constant and may differ from the steam temperature
8. Scattering is negligible
9. Uniform radiosity is assumed.

Fluid conditions required by the model include local vapor temperature, void fraction, pressure, and droplet density, size, and temperature. Rod group conditions include the number of groups, group view factors, mean beam lengths, emissivities, and surface temperatures. With these inputs, the radiative heat transfer package[10] will calculate the radiative heat transfer to the vapor, droplets, and channel wall, in addition to the net surface radiative heat flux for each rod group. Although Equation (44) could have been used, it was felt to be realistic to allow for droplet breakup. Thus, the characteristic droplet size was calculated using a critical Weber number criterion,

$$We_{crit} = \frac{\rho_v (u_v - u_\ell)^2 \delta}{\sigma g_c} \quad . \tag{48}$$

Phase velocities are normally calculated from the local fluid properties and conditions. To avoid numerical difficulties as the mass flux approaches zero, MAYU-4b calculates the relative velocity as

$$u_v - u_\ell = \frac{j_g}{\langle\alpha\rangle} - \frac{j_f}{1-\langle\alpha\rangle}$$

$$= \frac{1}{\langle\alpha\rangle(1-\langle\alpha\rangle)} \left[(1-\langle\alpha\rangle) j_g - \langle\alpha\rangle j_f\right]$$

$$= \frac{(u_g - j)}{(1-\langle\alpha\rangle)} \tag{49a}$$

or, from the definition of drift velocity (V_{gj}),

$$u_v - u_\ell = \frac{V_{gj}}{1-\langle\alpha\rangle} \ . \tag{49b}$$

Selecting a critical Weber number of 11.0, the droplet diameter (δ) is given by

$$\delta = \frac{11\sigma g_c}{\rho_v V_{gj}^2} (1-\langle\alpha\rangle)^2 \tag{50}$$

and under the assumption of a constant size droplet, the droplet density number is given by

$$N_d = \frac{6(1-\langle\alpha\rangle)}{\pi\delta^3} \ . \tag{51}$$

The governing equation for net radiative heat flux from a surface was derived using an approach similar to that used by Siegel and Howell.[11] For a gray gas, Mandell found the resulting set of equations to be

$$\sum_{k=1}^{N} \sum_{j=1}^{N} \left[\frac{\delta_{kj}}{\varepsilon_j} - F_{k_j} \frac{(1-\varepsilon_j)}{\varepsilon_j} \tau_{k_j}\right] q_j'' = \sum_{k=1}^{N} \sum_{j=1}^{N} \left[(\delta_{k_j} - F_{k_j} \tau_{k_j}) \sigma T_j^4 \right.$$

$$\left. - \varepsilon_{k_j}^v F_{k_j} \sigma T_v^4 - \varepsilon_{k_j}^L F_{k_j} \sigma T_L^4\right] \ . \tag{52}$$

The liquid and vapor radiative properties can be found in Mandell's report[10] along with the group view factor calculations.

To find the radiative heat transfer from the surfaces to the vapor and droplets, consider two surfaces with a gray fluid between. The total radiant energy leaving surface-k is $B_k A_k$, where B_k is the radiosity and A_k is the area of surface-k. The amount of energy reaching surface-j is given by

$$B_k A_k F_{k_j} \tau_{k_j},$$

and the amount absorbed by the vapor is

$$B_k A_k F_{k_j} \alpha_{k_j}^v \ .$$

The radiant energy emitted by the vapor is

$$A_k F_{k_j} \varepsilon_{k_j}^v \sigma T_v^4,$$

so the net energy absorbed by the vapor is

$$q_v = A_k F_{k_j} (\alpha^v_{k_j} B_k - \varepsilon^v_{k_j} \sigma T_v^4) \quad . \tag{53}$$

The total net radiative heat transfer to the vapor is obtained by summing over all surfaces,

$$q_v = \sum_{j=1}^{N} \sum_{k=1}^{N} A_k F_{kj} [\alpha^v_{kj} B_k - \varepsilon^v_{kj} \sigma T_v^4] \quad . \tag{54}$$

Similarly, the total net radiative heat transfer to the droplets is given by

$$q_\ell = \sum_{j=1}^{N} \sum_{k=1}^{N} A_k F_{kj} [\alpha^L_{kj} B_k - \varepsilon^L_{kj} \sigma T_L^4] \quad . \tag{55}$$

Thus, the radiative heat transfer to the droplets results in an additional volumetric vapor generation term, given by

$$\Gamma_{rad} = \frac{(q_\ell)_{rad}}{A_{xs} \Delta z \, h_{fg}} \quad . \tag{56}$$

Radiation Model Verification

Verification of the radiative heat transfer model's compatibility with the revised MAYU code was made by comparing the code's calculations with data from the BWR emergency core cooling tests conducted in the GOTA test loop at Studsvik Energiteknik AB in Sweden.[12] The radiation-only experiments under consideration here consisted of the application of a constant power level (49 kW) to a natural convection (air) cooled, electrically heated, full-scale, 64-rod bundle. Water cooling was supplied to the outside of the bundle canister to establish a boundary condition. The rod local peaking factors are shown in Figure 12, along with the six rod groups selected.

Several approximations were made in the simulation attempt:

1. Only the midplane power section, 1.3 ft in length, was considered.

2. Air cooling via natural circulation was approximated in MAYU-4b by steam with an inlet enthalpy of 1700 Btu/lbm and an inlet mass flux of 500 lbm/hr-ft^2. At atmospheric pressure, this corresponds to vapor temperature of 1540°F. Fortunately, parametric runs have indicated that, below a certain flow rate, the predicted results are insensitive to the inputs assumed.

3. The rod bundle was broken into six rod groups and one channel wall surface. The water rod was grouped with active rods.

4. All rods were assumed to be of the same diameter, although 12 corner and adjacent-to-corner rods in the ASEA-ATOM test bundle were of a slightly smaller diameter.

Rod and channel wall emissivities were set at 0.65, as determined by the experimenters. Calculated rod temperatures are shown in Figure 13, along with the range of temperatures measured for the rods in each group. It can be seen that agreement between the radiation model in MAYU-4b and the Studsvik data is fairly good, however; the model obviously predicts too much radiation heat transfer in the bundle interior and too little from the outer rods.

6 (0.998)	5 (1.004)	5 (0.997)	5 (1.205)	5 (1.094)	5 (1.101)	5 (0.897)	6 (0.997)
5 (1.101)	4 (1.020)	3 (1.088)	3 (1.002)	3 (0.900)	3 (0.899)	4 (1.004)	5 (0.902)
5 (1.111)	3 (1.195)	2 (1.004)	2 (0.896)	2 (0.901)	2 (0.294)	3 (0.897)	5 (1.096)
5 (1.093)	3 (1.094)	2 (0.908)	1 (0.900)	1 (0.0)	2 (0.901)	3 (0.902)	5 (1.096)
5 (1.101)	3 (1.098)	2 (0.900)	1 (0.905)	1 (0.903)	2 (0.905)	3 (1.008)	5 (1.198)
5 (1.198)	3 (1.101)	2 (0.296)	2 (0.903)	2 (0.903)	2 (1.008)	3 (1.092)	5 (0.997)
5 (0.897)	4 (1.003)	3 (1.102)	3 (1.099)	3 (1.100)	3 (1.202)	4 (1.010)	5 (1.007)
6 (1.096)	5 (0.897)	5 (1.193)	5 (1.094)	5 (1.098)	5 (1.096)	5 (1.100)	6 (1.002)

Numbers 1 through 6 refer to rod group; numbers in parenthesis are the rod power factors.

INEL 2 0490

Figure 12. Radiation model verification rod grouping and power factors, Studsvik data[12].

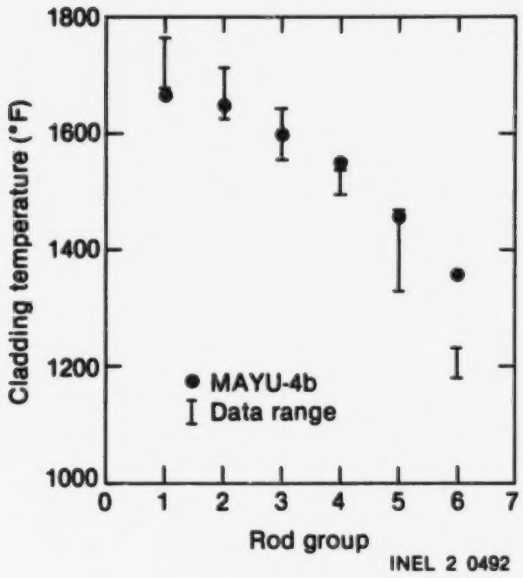

Figure 13. Comparison of MAYU-4b and experimental results[12].

It is felt that this prediction capability is acceptable; however, future improvements could be easily made using a photon scattering correction factor. Model improvements of this type have been found[13] to improve the predictive capabilities of radiation models such as that used in MAYU-4b.

BWR INLET FLOW BLOCKAGE SIMULATION

A best-estimate simulation of a BWR inlet flow blockage accident was performed using MAYU-4b. In accordance with previous investigations,[14] 5.4% of the initial inlet flow was assumed to enter the bundle as leakage inflow. The power was decayed to 82% of the initial power in 1.8 s. This is based on detailed physics calculations performed at the Idaho National Engineering Laboratory.[15] Parametric runs indicated that spacer effects were not important for BWR inlet flow blockage, so the spacer model was not utilized. The user input rewet temperature was set at $T_w - T_{sat} = 180°F$, as recommended by Mayinger.[16] The General Electric Company Brunswick design was chosen for the simulation due to its relatively flat radial power distribution (see Appendix C). The local power factors (for 7000 MWd/t) are shown in Figure 14, along with the rod groups chosen. Input information and user code input are presented in Tables 3 and 4, respectively. The resulting output at 0 and 1 s is shown in Appendix D.

The results of the BWR fuel bundle simulation are presented in Figures 15 through 18. A discussion of these graphs is presented below:

1. Figure 15 shows the cladding surface temperature of the hottest rod group as a function of axial position and time. The axial location of the peak cladding temperature (PCT) was found to vary with time. Early in the transient the highest temperatures are near the top of the bundle, where dryout starts. The location of the PCT then moves toward the midplane level, where the power is the greatest. As the bundle becomes increasingly liquid deficient above the dryout point, the PCT once again moves downstream. This can be explained by looking at the plots of vapor temperature versus axial position in Figure 16. It is seen that the highest vapor temperatures are consistently downstream of the PCTs, resulting in a deterioration of the convective heat transfer immediately downstream of the PCT. As a result, the PCT migrates downstream. It is also interesting to compare the axial changes in cladding temperature between 20 and 60 s. As can be noted in Figure 15, the temperatures near the top of the bundle have increased much more than those near the midplane. This is due to the heat transfer from the vapor to the rods at this (lower power) location. Indeed, for a 20-s period starting about 7 s into the transient, the vapor temperatures near the exit are actually higher than the cladding temperatures, resulting in a reversal in direction of the convective heat flow. After about 30 s into the transient, however, the cladding temperatures are consistently higher than the vapor temperatures, even at the exit.

2. Figure 16 presents the vapor temperature profiles for various times. The temperature rise slows as the cladding temperature excursion slows. The maximum vapor temperature is consistently downstream of the PCT location.

3. Figure 17 shows the void fraction profiles as a function of time. The boiling boundary moves to the inlet as the saturated leakage inflow replaces the subcooled inlet flow. The void fraction above the dryout location (near the 3-ft level) increases from 8 to 60 s as the vapor becomes increasingly superheated. The decrease below the dryout front from 8 to 60 s is caused by the power decrease.

4. Figure 18 presents the fuel centerline temperature histories. The decrease below the dryout point is once again caused by the decrease in bundle power. Although the power ramp occurs in the first 1.8 s, the thermal inertia of the rod causes a delay in the fuel temperature response. Above the dryout location, the fuel centerline temperature increases as the transient progresses. As expected, the maximum occurs at the midplane, where the power is highest.

The analysis just discussed indicates that, for the conditions assumed, there will be no liquid fallback from the upper plenum, and that fuel melting would be expected for a complete blockage of the inlet of a BWR fuel rod bundle.

1 6 (1.000)	2 6 (1.012)	3 6 (1.029)	4 6 (0.990)	5 6 (0.972)	6 6 (0.981)	7 6 (1.020)	8 6 (1.020)
9 6 (1.012)	10 5 (0.945)	11 4 (1.097)	12 4 (1.043)	13 4 (1.016)	14 4 (1.021)	15 4 (1.074)	16 6 (0.952)
17 6 (1.029)	18 4 (1.097)	19 3 (0.985)	20 3 (0.943)	21 2 (1.090)	22 2 (1.057)	23 5 (0.936)	24 6 (1.091)
25 6 (0.990)	26 4 (1.043)	27 3 (0.943)	28 1 (0.950)	29 6 (0.0)	30 2 (1.015)	31 5 (1.024)	32 6 (1.019)
33 6 (0.972)	34 4 (1.016)	35 2 (1.090)	36 6 (0.0)	37 1 (1.030)	38 3 (0.955)	39 5 (0.808)	40 6 (0.997)
41 6 (0.981)	42 4 (1.021)	43 2 (1.057)	44 2 (1.015)	45 3 (0.955)	46 3 (0.944)	47 5 (1.004)	48 6 (1.015)
49 6 (1.020)	50 4 (1.074)	51 5 (0.936)	52 5 (1.024)	53 5 (0.808)	54 5 (1.004)	55 5 (0.931)	56 6 (0.945)
57 6 (1.020)	58 6 (0.952)	59 6 (1.091)	60 6 (1.019)	61 6 (0.997)	62 6 (1.015)	63 6 (0.945)	64 6 (0.961)

Rod Group	Number of Rods	Power Factor (based on 64 active)
1	2	1.0219
2	6	1.0880
3	6	0.9850
4	10	1.0841
5	10	0.9724
6	30	0.9652

Numbers in upper left corner of boxes are rod numbers; centered numbers refer to rod group; and numbers in parentheses are rod power factors.

INEL 2 0489

Figure 14. 8 x 8 BWR fuel simulation—rod grouping and power factors at 7000 MWd/t.

Table 3. Input information for BWR simulation

Data	Pressure	=	1046 psia
	Power	=	6750 kW, t = 0 s 5535 kW, $t^a \geq 1.8$ s
	Inlet enthalpy	=	524.1 Btu/lbm, t = 0 s 549.58 Btu/lbm, $t^a \geq 0.05$ s
	Inlet mass flux	=	1,112,290 lbm/hr-ft^2, t = 0 s 60,163.6 lbm/hr-ft^2, $t^a \geq 0.05$ s
	Axial power shape	=	1.38 P/A chopped cosine
	Heated length	=	12.5 ft
	Flow area	=	0.10726 ft^2
	Hydraulic diameter	=	0.435512 ft
	Channel width	=	5.278 in.
	Rod pitch	=	0.641 in.
	Rod outside diameter	=	0.483 in.
	Rod inside diameter	=	0.419 in.
	Number of fuel rods	=	64

a. Linear decrease from initial value to final value over time interval shown.

Table 4. User input for BWR fuel simulation

```
)
 &MYUINP
  AXPEAK(1,1) = 0.0, 1.0417, 2.0833, 3.125, 4.1667, 5.2083,
                6.25, 7.2917, 8.3333, 9.375, 10.4167, 11.4583,
                12.51,
  AXPEAK(1,2) = 0.2925, 0.5938, 0.8596, 1.0815, 1.2518, 1.3537,
        1.3889, 1.3537, 1.2518, 1.0815, 0.8596, 0.5938, 0.2925,
  AXSI(1,1) = 0.0, 12.51,
  AXSI(1,2) = 2*1.0,
  ICCFL = 3, PKWREF = 1.0, KPZ = 1, KPR = 1,
  CLDPWR = 0.0, BTPKW = 2*1.0, IFRICT = 0,
  ROCL = 0.2415, RICL = 6*0.2095, ITCONS = 1,
  CCFLA = 0.080445, DHYD = 0.0435512, FLOWA = 0.10726,
  FLNGTH = 12.5, IDEBUG = 0, IVOID = 3,
  TMAX = 60., CCFLCN = 1.0, 1.789,
  MINDT = 1, XCCON = 2*0.0,  DTMAX = 0.025, DTWET = 180.,
  TITLE = 36H BWR INLET FLOW BLOCKAGE RUN,
  JZ = 25, NRODS = 6,
  LBLROD(1,1) = 8H28,37    ,
  LBLROD(1,2) = 8H21,22,..,
  LBLROD(1,3) = 8H19,20,..,
  LBLROD(1,4) = 8H11,12,..,
  LBLROD(1,5) = 8H10,23,..,
  LBLROD(1,6) = 8H1,2,3,..,
  ISPACE = 0,
  POWRI(1,1) = 0.0, 1.8, 61.0,
  POWRI(1,2) = 6750.0, 2*5535.0,
  ENTHI(1,1) = 0.0, 0.05, 61.0,
  ENTHI(1,2) = 524.1, 2*549.58,
  PRESI(1,1) = 0.0, 61.0,
  PRESI(1,2) = 2*1046.0,
  GFLXI(1,1) = 0.0, 0.05, 61.0,
  GFLXI(1,2) = 1112290.0, 2*60163.66,
  RPEAK = 6*1.00,
  PLOCAL = 1.0219, 1.088, 0.9850, 1.0841, 0.9724, 0.9652,
  PNTYPE = 2, 6, 6, 10, 10, 30,
  LOCPLT = 103, 104, 105, 106, 107, 108, 109, 110, 111,
      112, 113, 114, 115, 116, 117, 118, 119, 120, 121, 122,
      123, 124, 125, 126,
  LOCROD(1,1) = 4, 6, 8, 10, 12, 14, 16, 18, 22, 26,
  LOCROD(1,2) = 4, 6, 8, 10, 12, 14, 16, 18, 22, 26,
  LOCROD(1,3) = 4, 6, 8, 10, 12, 14, 16, 18, 22, 26,
  LOCROD(1,4) = 4, 6, 8, 10, 12, 14, 16, 18, 22, 26,
  LOCROD(1,5) = 4, 6, 8, 10, 12, 14, 16, 18, 22, 26,
  LOCROD(1,6) = 4, 6, 8, 10, 12, 14, 16, 18, 22, 26,
  IROD = 9*6, 5, 5*4, 2*6, 4, 2*3, 2*2, 5, 2*6, 4, 3, 1, 6,
      2, 5, 2*6, 4, 2, 6, 1, 3, 5, 2*6, 4, 2*2, 2*3, 5, 2*6,
      4, 5*5, 9*6, 32*7,
  EMSVTY(1,1) = 6*0.90,
  EMSVTY(1,2) = 6*0.65,
  BETA2 = 1.0, INSURF = 0, IRADCK = 0, IRADHT = 1, IRADPR = 1,
  CHANW = 5.278, RPITCH = 0.641,
  RELAX(1,1) = 50.0, 500.0,
  RELAX(1,2) = 0.1, 0.5,
  ECHANW = 0.70, NROD = 8, IREACT = 1,
 &END
)LAST
```

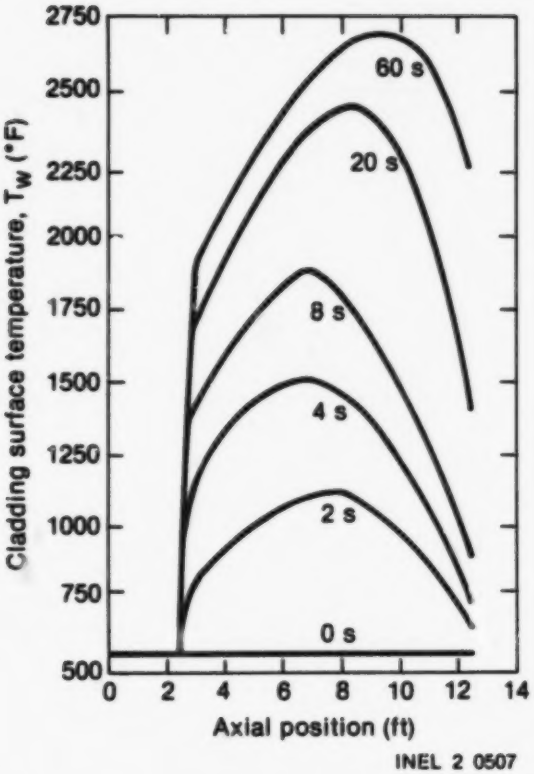

Figure 15. Simulated BWR cladding surface temperature as a function of axial position and time.

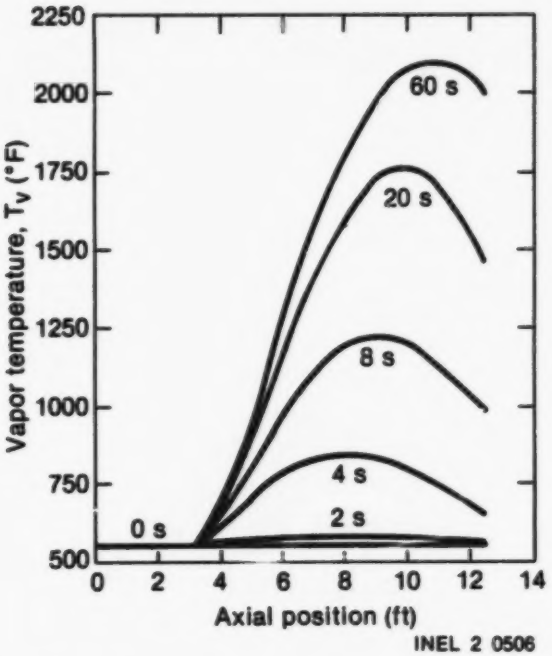

Figure 16. Simulated BWR vapor temperature profiles as a function of axial position and time.

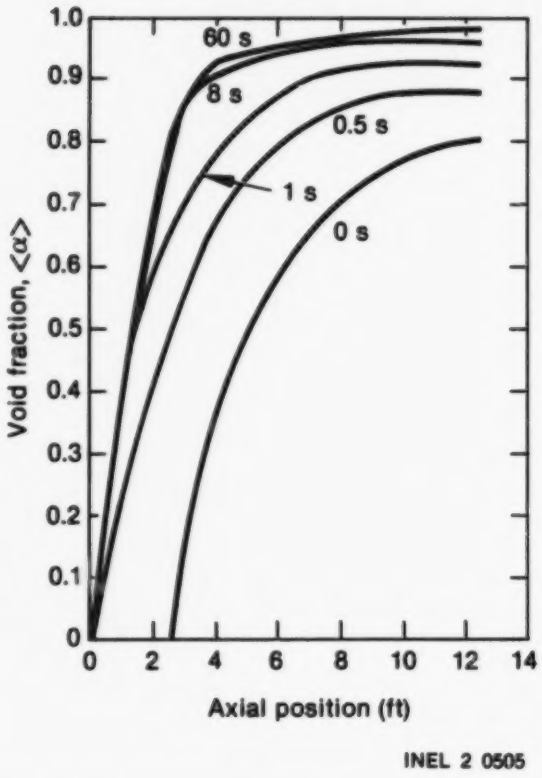

Figure 17. Simulated BWR void fraction profiles as a function of axial position and time.

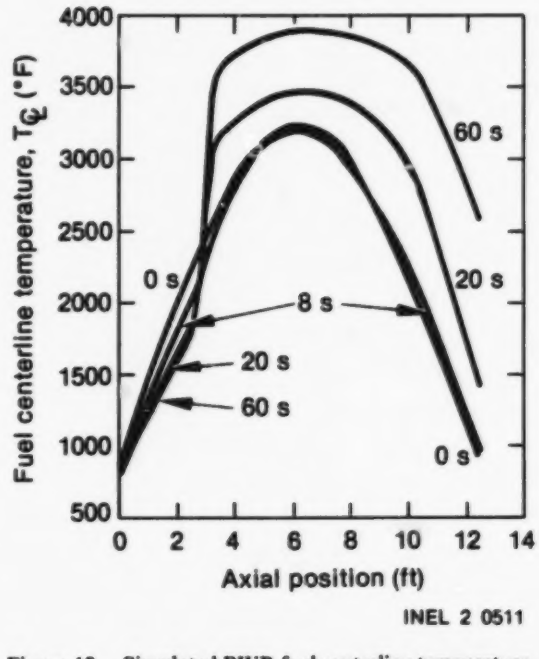

Figure 18. Simulated BWR fuel centerline temperature histories as a function of axial position and time.

PARAMETRIC RUNS AND RESULTS

The MAYU-4b runs were made with 3- and 12-ft cores to investigate the ability of the Power Burst Facility (PBF) to simulate the inlet flow blockage of a BWR fuel rod bundle. In both cases, a uniform axial power profile was used. All rods were given the same peaking factor and the zircaloy/water reaction rate model was bypassed. The input information and code user input are shown in Tables 5 and 6.

The 12-ft run was performed first to investigate the heat transfer mechanisms present in a full-length bundle. As before, 5.4% of the initial inlet mass flux was assumed to enter the bundle, as leakage flow, in the case of 100% blockage of the inlet orifice. This leakage rate is in agreement with earlier investigations.[14] Since this leakage flow is from the core bypass (i.e., interstitial) region, it was assumed to be at saturated temperature. The results indicated that this inflow rate was sufficiently high that no countercurrent flow occurred anywhere in the bundle during the blockage transient.

Table 5. Input information for parametric runs

Data for 12-ft Run	Pressure	=	1046 psia
	Power	=	6042 kW $t \geq 0$ s
	Inlet enthalpy	=	524.1 Btu/lbm, $t = 0$ s 549.58 Btu/lbm, $t^a > 0.05$ s
	Inlet mass flux	=	1,112,290.0 lbm/hr-ft^2, $t = 0$ s 60,163.66 lbm/hr-ft^2, $t^a = 0.05$ s
	Axial power shape	=	uniform axial
	Flow area	=	0.10843612 ft^2
	Hydraulic diameter	=	0.4840 ft
	Channel width	=	5.2718 in.
	Rod pitch	=	0.65 in.
	Rod outside diameter	=	0.5625 in.
	Rod inside diameter	=	0.5187 in.
	Number of fuel rods	=	49
Changes for 3-ft Run	Power	=	1,888.1 kW $t \geq 0$ s
	Inlet mass flux	=	1,112,290.0 lbm/hr-ft^2, $t = 0$ s 30,081.83 lbm/hr-ft^2, $t^a > 0.05$ s

a. Linear decrease from initial to final value over time interval shown.

Table 6. User input for 12 ft run

```
)
 &MYUINP
  AXPEAK(1,1) = 0.0, 12.01,
  AXPEAK(1,2) = 2*1.0,
  AXSI(1,1) = 0.0, 12.01,
  AXSI(1,2) = 2*1.0,
  DTMAX = 0.025,
  ICCFL = 3, PKWREF = 1.0,
  KPR = 1, CLDPWR = 0.0,  KPZ = 1,
  BTPKW = 2*1.0, IFRICT = 0,
  ROCL = 0.28125, ITCONS = 1,
  CCFLA = 0.0989, TMAX = 60.,
  IDEBUG = 0, IVOID = 3,
  CCFLCN = 1.0, 1.789,  MINDT = 1,
  TITLE = 36H INLET FLOW BLOCKAGE 1 ROD GROUP,
  DHYD = 0.04840, FLOWA = 0.10843612,
  FLNGTH = 12.0, RICL = 0.25935,
  JZ = 24, NRODS = 1, XCCON = 2*0.0,
  LBLROD(1,1) = 8H1,2,3,..,
  ISPACE = 0,
  POWRI(1,1) = 0.0, 1.8, 61.0,
  POWRI(1,2) = 3*6042.0,
  ENTHI(1,1) = 0.0, 0.05, 61.0,
  ENTHI(1,2) = 524.1,2*549.58,
  PRESI(1,1) = 0.0, 61.0,
  PRESI(1,2) = 2*1046.0,
  GFLXI(1,1) = 0.0, 0.05, 61.0,
  GFLXI(1,2) = 1112290.0, 2*60163.66,
  RPEAK = 1.0, PLOCAL = 1.0, PNTYPE = 49,
  LOCROD(1,1) = 4,7,10,13,15,17,19,21,23,25,
  LOCPLT = 103,104,105,106,107,108,109,110,111,112,113,
       114,115,116,117,118,119,120,121,122,123,124,125,
  IROD = 49*1, 28*2, ECHANW = 0.70, NROD = 7,
  EMSVTY(1,1) = 0.90,
  EMSVTY(1,2) = 0.65,
  BETA2 = 1.0, INSURF = 0,
  IRADCK = 0, IRADHT = 1, IRADPR = 1,
  CHANW = 5.271768, RPITCH = 0.65,
  RELAX(1,1) = 50.0, 500.0,
  RELAX(1,2) = 0.1, 0.5,
 &END
)LAST
```

If a 3-ft core is to properly simulate the thermal-hydraulic performance of a full-length core, it is imperative that the heat transfer mechanisms be similar. Thus we seek conditions such that the exit qualities are similar and the 3-ft bundle only experiences co-current flow. A steady state energy balance on the control volume, shown in Figure 19, yields.

$$G A_{xs} (h_f + x_e h_{fg}) = G A_{xs} h_{in} + \overline{q''} P_H L_H \quad . \tag{57}$$

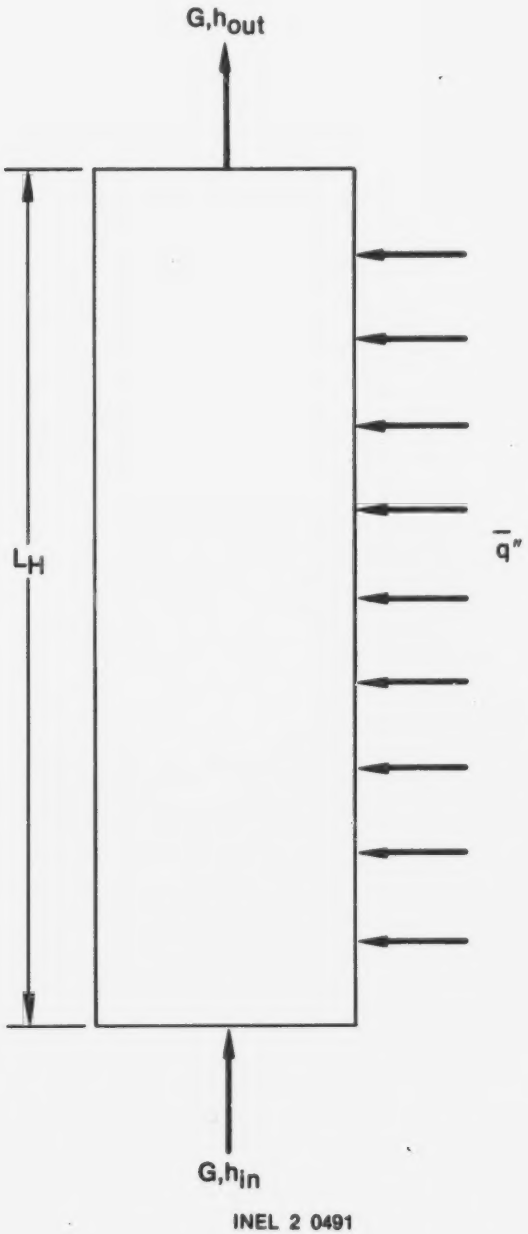

Figure 19. Control volume for steady state energy balance.

For a saturated inlet, the equilibrium quality at the exit is

$$x_e = \frac{\overline{q''} P_H L_H}{G A_{xs} h_{fg}} . \quad (58)$$

For bulk boiling conditions,

$$x_e = \langle x \rangle = \frac{\rho_g j_g}{G} . \quad (59)$$

Combining Equations (58) and (59),

$$j_g = \frac{\overline{q''} P_H L_H}{\rho_g h_{fg} A_{xs}} . \quad (60)$$

From Equation (58), it can be seen that decreasing the heated length by a factor of 4 will change the exit quality unless the factor (q''/G) is made 4 times as large. By replacing L_H in Equation (60) with an arbitrary axial position, z, it is also evident that an increase in the heat flux causes an increase in the local vapor velocity $j_g(z)$, which implies that if countercurrent flow does not occur at a given power level, it will not occur for a higher one.

Several short computer runs were performed to scope various combinations of ($\overline{q''}/G$). To simply increase the heat flux by a factor of 4 is not experimentally feasible. On the other hand, decreasing the inlet mass flux by a factor of 4 is also unacceptable. Indeed, in both cases, a boiling transition was experienced for the initial conditions. Clearly, it would be unacceptable to initiate an inlet flow blockage event from conditions in which the bundle was already in film boiling.

After much study it was decided that an increase in heat flux of 25%, accompanied by a decrease in leakage inflow of 50%, would not cause a boiling transition prior to the transient and yet would give a reasonable case for comparison with the 12-ft run, even though these conditions result in different exit qualities.

The results of these two runs are presented in Figures 20 through 29. A discussion of these results is presented below:

1. Figure 20 presents the vapor temperatures as a function of position and time for both the 12- and 3-ft runs. The vapor temperature increases significantly above the dryout point for the 12-ft bundle, but the shorter bundle does not have enough heated length above the dryout point to increase the vapor superheat significantly.

2. Figure 21 shows the void fraction for the 12-ft run as a function of time and position. The boiling boundary moves to the inlet as the (saturated) leakage inflow replaces the higher (subcooled) inlet flow. At 1 s into the transient, the decrease in inlet mass flux has resulted in a much higher void fraction throughout the bundle. It can be observed that at 8 s, the void fraction is lower than at 1 s for the lower part of the bundle. This can be explained by considering the movement of the dryout location early in the transient. After 1 s the dryout point is near the 4-ft level and is still dropping. Notice how flat the void profile is above this point, indicating that the vapor temperature has not yet increased enough to cause significant evaporation of the droplets. Soon thereafter, the dryout point reaches its final location at the 2-ft level. From this time on, the void fraction profile increases monotonically with time above the dryout point as the vapor temperature increases.

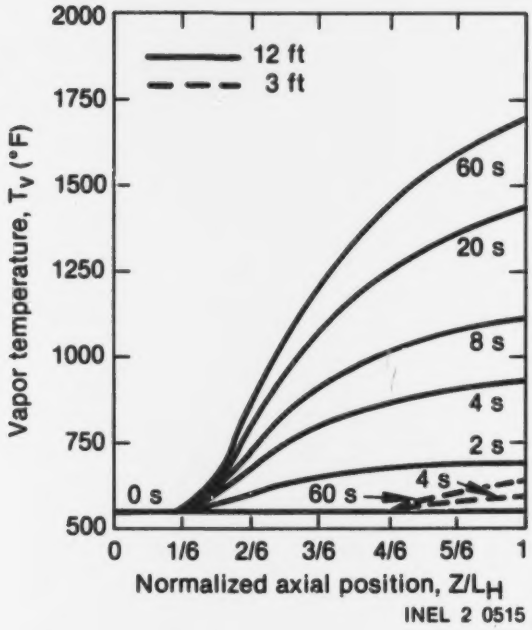

Figure 20. Vapor temperatures as a function of position and time for both runs.

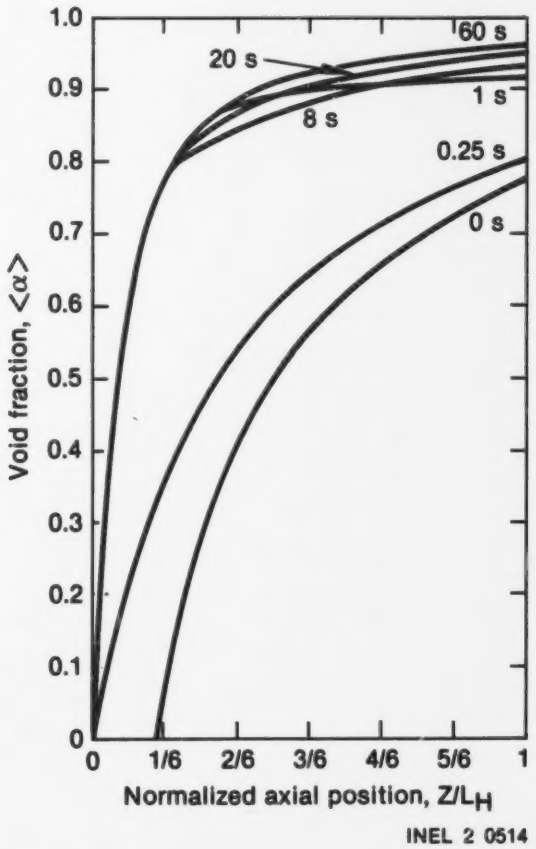

Figure 21. Void fraction for the 12-ft run as a function of time and position.

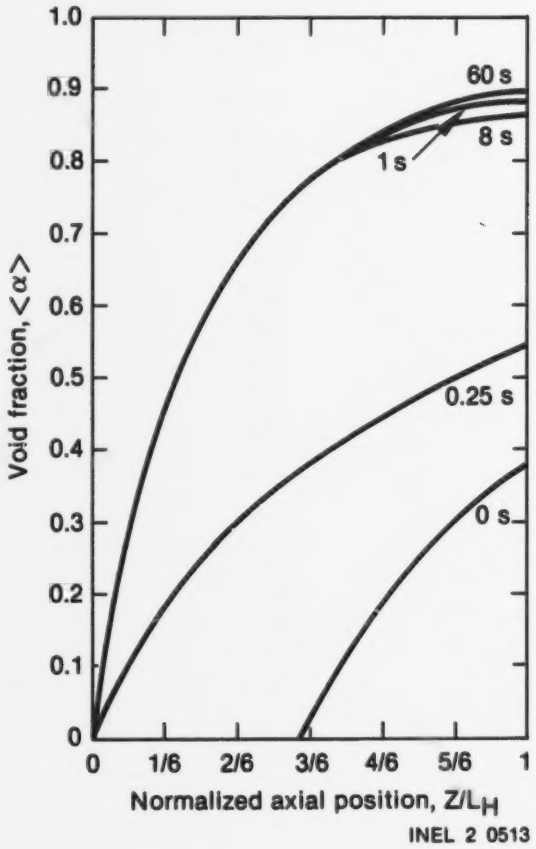

Figure 22. Void fraction as a function of time for the 3-ft run.

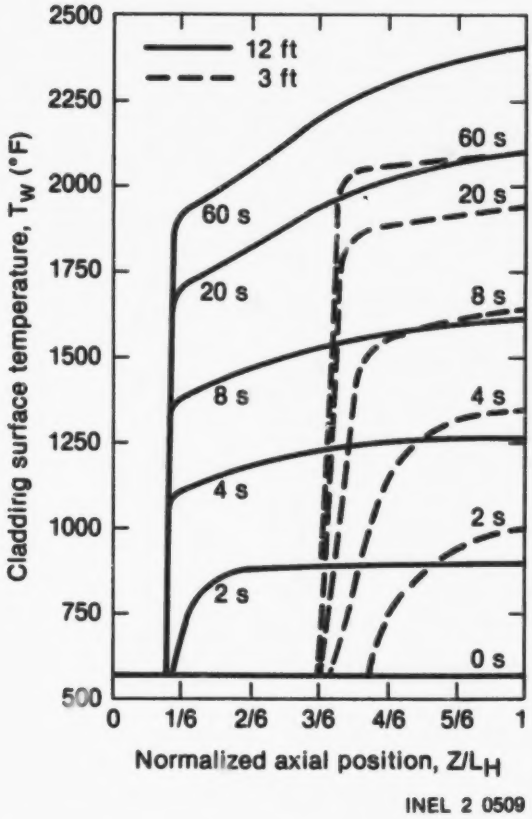

Figure 23. Axial cladding surface temperature profiles as a function of time for both runs.

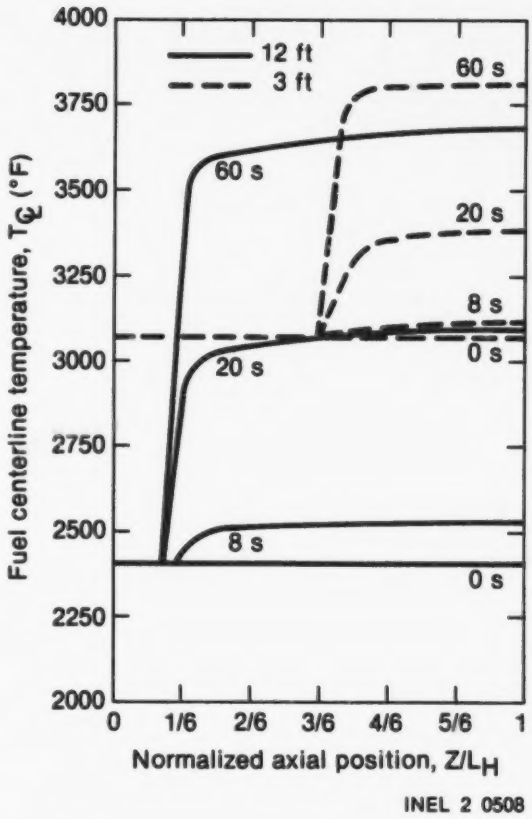

Figure 24. Fuel centerline histories for both runs.

3. Figure 22 shows the void fraction profile as a function of time for the 3-ft run. The response is similar to the 12-ft case; however, the exit void fraction is consistently lower than in the full-length bundle. This is due to the much lower vapor superheats in the shorter bundle.

4. Figure 23 presents the axial cladding surface temperature profiles versus time for both runs. Initially, the temperature excursion is more severe for the 3-ft case. This is to be expected because of the larger linear heat rate. However, the cladding temperatures at the higher elevations of the 12-ft bundle eventually surpass those of the 3-ft bundle. This can be explained by considering the heat transfer mechanisms near the exits. In the 12-ft bundle, the vapor temperature has increased significantly, causing the convective heat transfer from the rods to the vapor to decrease. In the 3-ft bundle, the vapor temperature has not increased enough to strongly affect the convective component. Finally, it is interesting to note that the exit (3-ft) temperatures are consistently higher than those at the 3-ft level of the 12-ft bundle. Once again, this is due to the higher linear heat rate.

5. Figure 24 displays the fuel centerline temperature histories for both runs. The centerline temperature for the 3-ft run is higher throughout the transient as a result of the higher linear heat rate. However it appears that the temperatures of the 3-ft bundle will fall below those of the 12-ft bundle at a later time. A comparison of the energy balances of these two bundles reveals that a smaller fraction of the rod power goes to storage in the 3-ft bundle. The lower vapor temperatures and void fractions are responsible for this decrease in storage, and the resultant lower heatup rate.

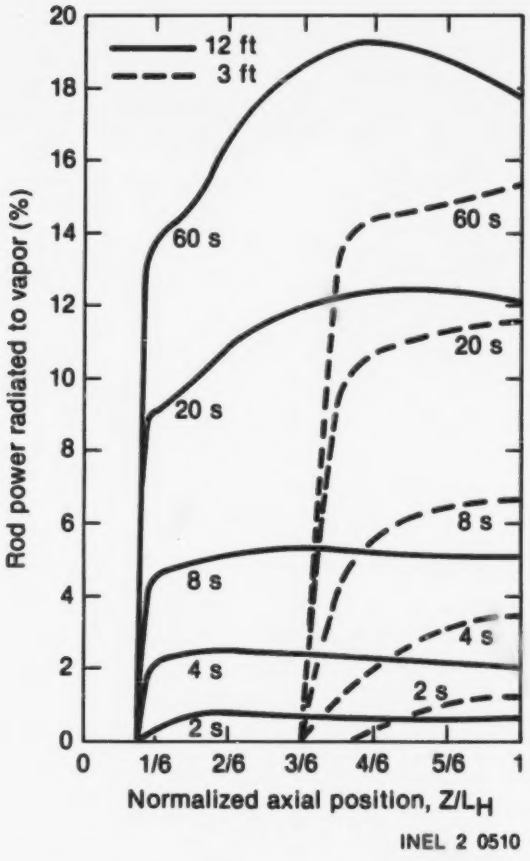

Figure 25. Fraction of bundle power radiated to the vapor as a function of time and position for both the 3- and 12-ft bundles.

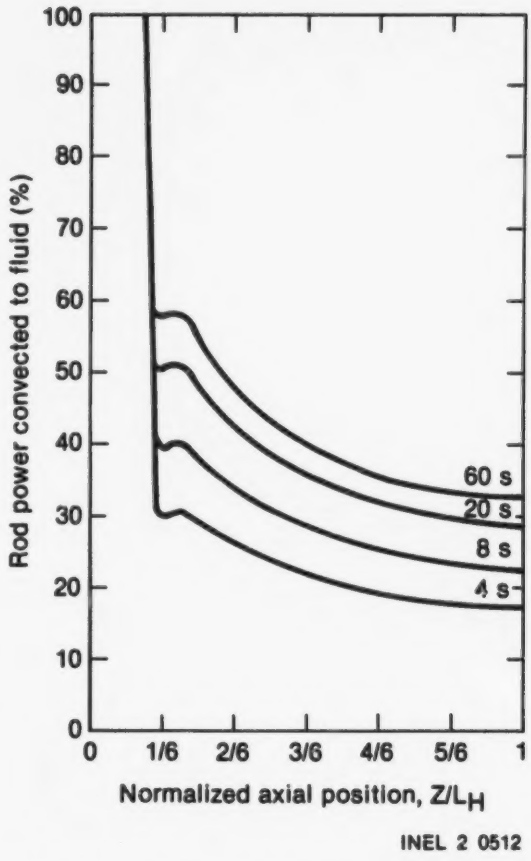

Figure 26. Fraction of bundle power convected to the fluid for the 12-ft bundle.

6. Figure 25 shows the fraction of bundle power radiated to the vapor for both bundles as a function of time and position. It can be seen that the heat transferred due to radiation is appreciable. As might be expected, the profiles are similar to the cladding temperature plots. Radiative heat transfer is dependent on the temperature differences; hence, the power radiated to the vapor increases as the cladding surface temperatures increase. The decrease at the higher elevations of the 12-ft bundle are due to the higher vapor temperatures.

7. Figures 26 and 27 compare the fraction of the bundle power convected to the fluid for the 12- and 3-ft bundles, respectively. The percentages near the exit are consistently higher for the 3-ft case, reflecting the lower vapor superheat. Note, however, that the percentage for the 3-ft bundle at the exit is lower than the 3-ft level of the 12-ft bundle. This should be expected since the heat transfer coefficient in the PDO heat transfer regime is proportional to the vapor mass flux to the 0.8 power, and the flow quality is greater at the exit of the 3-ft bundle. For all plots except the 3-ft run at 60 s, there is a dip just beyond the dryout location. This can be explained by considering the implications of the nonequilibrium vapor generation. Early in the transient, there is negligible vapor generation at the dryout point and immediately downstream; hence, the vapor mass flux increases only slightly. As a result, the heat transfer coefficient is essentially constant in this region. Thus, the fraction of rod power convected to the fluid drops off sharply at, and just beyond, the dryout point. This energy goes into storage, thus causing the fuel to heat up. As we move downstream, the vapor

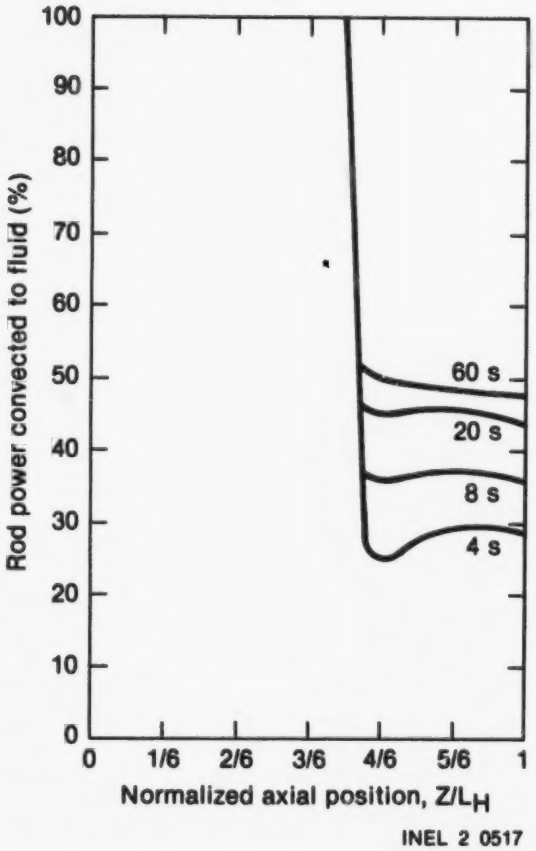

Figure 27. Fraction of bundle power convected to the fluid for the 3-ft bundle.

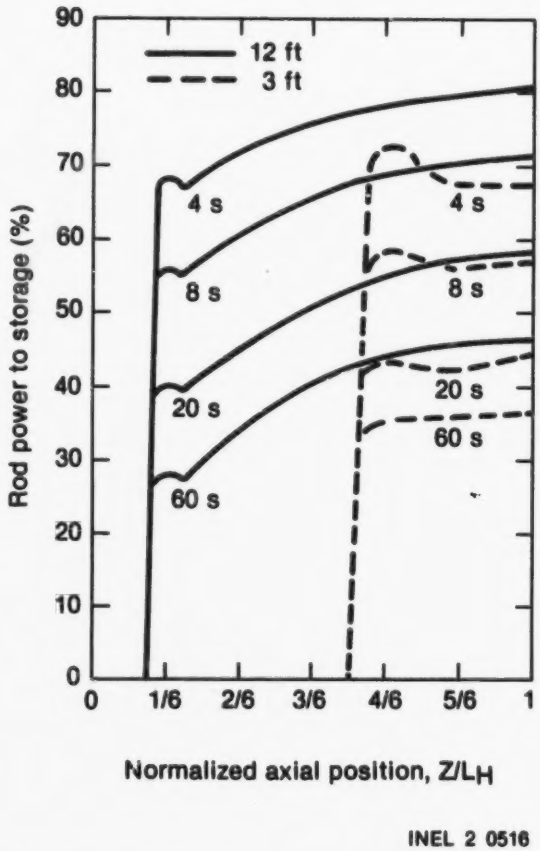

Figure 28. Fraction of bundle power going to storage for both bundles.

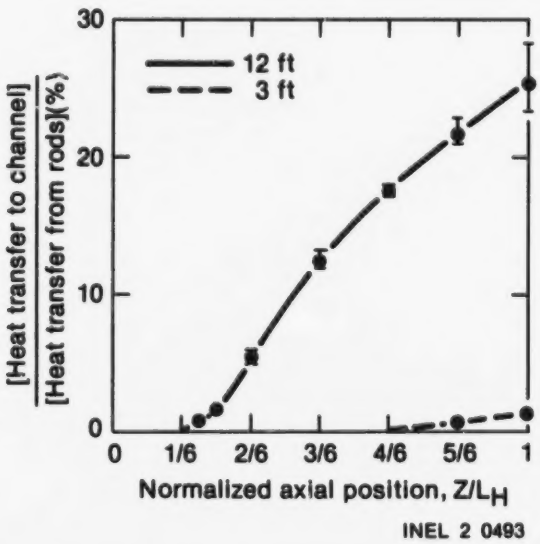

Figure 29. Fraction of total heat transfer from rods to channel wall for both bundles.

superheat increases, which increases the vapor velocity, and thus the heat transfer coefficient. This causes the observed increase in convection heat transfer. As we move further downstream, the vapor superheat increases faster than the vapor velocity, and thus the convective heat transfer falls off again. Later in the transient, the vapor temperature immediately downstream of the dryout point has increased, making the dip less noticeable (at least for the 3-ft bundle). However, it is still present due to the accompanying increase in vapor-mass flux. At 60 s into the higher power (3-ft) run, the vapor temperature is finally high enough that the dip has disappeared.

8. Figure 28 shows the fraction of bundle power going to storage. This reflects the amount of energy not transferred by convective or radiative heat transfer, and it is the driving force for rod heatup. The lower storage in the 3-ft bundle is responsible for the slower heatup seen in Figure 24. Also note the dips that are out-of-phase (as they should be) with those in Figures 26 and 27.

9. Figure 29 displays the fraction of the total heat transfer from the rods that goes to the channel wall, either through convection from the vapor or from radiative heat transfer. It is interesting to note that the plots are practically constant with time (results contained within bars for all times), reflecting the fact that all but a few percent of the heat transfer to the wall is due to convection. It is apparent that the heat transferred to the channel wall is appreciable. This implies that more care should be taken in future studies in evaluating the inside surface temperature of the channel wall (taken here as saturation temperature).

Radiation heat transfer to the droplets was not plotted, as it was found to be typically less than 2% of the total heat transfer from the rods.

SUMMARY AND CONCLUSIONS

The computer code MAYU-4b appears to be well suited for the analysis of degraded core events such as a BWR inlet flow blockage. The only fundamental problems encountered during its usage are its relatively large expense and the fact that it often had mass conservation problems when ≤ 24 nodes were used for runs with countercurrent flows. It appears that this deficiency is correctable by using either more axial nodes or the addition of an iterative loop.

A best-estimate simulation using MAYU-4b indicated that fuel melting would occur in the event of complete inlet flow blockage of a BWR fuel rod bundle. Indeed, the results indicate that the expected leakage inflow is high enough to maintain a countercurrent-flow-limiting condition at the upper tie plate and thus prevent liquid fallback from the upper plenum. Although the peak centerline temperature had only reached 3900°F in 60 s, it appears that there is no additional heat transfer mechanism to prevent fuel melting.

Parametric studies performed with MAYU-4b indicate that it would be difficult to use the 3-ft Power Burst Facility core, with a single-phase inlet, to simulate an inlet flow blockage accident in a BWR. The results indicate that significant vapor superheat would be present at the higher elevations of a full-length core, whereas in the 3-ft core there is not enough heated length above the dryout location to cause appreciable vapor superheat. As a result, the thermal-hydraulic performance is somewhat different. The use of reduced inlet flow and/or a two-phase inlet would allow more superheat in a 3-ft bundle, although Figure 20 suggests that this may not be enough. Indeed, if dryout could be induced immediately downstream of the inlet, and the PBF channel(s) was insulated, it appears that there would still be insufficient heated length to attain the high superheats present near the exit of a full-length core. Nevertheless, although it does not appear possible to duplicate all aspects of a BWR inlet flow blockage accident in the PBF, it may well be possible to gain valuable information on fuel failure propagation modes and/or the potential for vapor explosions.

REFERENCES

1. W. C. Punches, *MAYU4 - A Method to Evaluate Transient Thermal-Hydraulic Conditions in Rod Bundles*, GEAP-23517, March 1977.

2. K. Ohkawa and R. T. Lahey, Jr., "The Analysis of CCFL Using Drift-Flux Models," *Nuclear Engineering and Design*, 61, 1980.

3. R. T. Lahey, Jr. and F. J. Moody, *The Thermal-Hydraulics of a Boiling Water Reactor*, ANS Monograph, 1977.

4. L. Baker and L. C. Just, *Studies of Metal-Water Reactions at High Temperatures III. Experimental and Theoretical Studies of the Zirconium-Water Reaction*, ANL-6548, May 1962.

5. P. Saha, B. S. Shiralkar, and G. E. Dix, "A Post-Dryout Heat Transfer Model Based on Actual Vapor Generation Rate in Dispersed Droplet Regime," ASME-77-HT-80, 1977.

6. N. A. Bailey, J. G. Collier, and J. C. Ralph, "Post Dryout Heat Transfer in Nuclear and Cryogenic Equipment," ASME-73-HT-16, 1973.

7. M. Ishii and M. A. Grolmes, "Inception Criteria for Droplet Entrainment in Two-Phase Cocurrent Film Flow," *AIChE Journal, 21*, 1975.

8. S. L. Soo, *Fluid Dynamics of Multiphase Systems*, Waltham, MA: Blaisdell Publishing Co., 1967.

9. A. W. Bennett, *Heat Transfer to Steam-Water Mixtures Flowing in Uniformly Heated Tubes in which the Critical Heat Flux has been Exceeded*, UKAEA Research Group Report AERE-R5373, 1967.

10. D. A. Mandell, *A Radiative Heat Transfer Model for the TRAC Code*, NUREG-CR-0994, November 1979.

11. R. Siegel and J. R. Howell, *Thermal Radiation Heat Transfer*, New York: McGraw-Hill Book Co., 1972.

12. L. Nilsson, L. Gustafson, and R. Harju, *Experimental Investigation of Cooling by Top Spray and Bottom Flooding of a Simulated 64-Rod Bundle for a BWR*, NORHAV S-046, 1978.

13. J. W. Spore, M. M. Giles, and R. W. Shumway, "A Best Estimate Radiation Heat Transfer Model Developed for TRAC-BD1," ASME-81-HT-68, 1981.

14. General Electric Staff, *Consequences of a Postulated Flow Blockage Incident in a Boiling Water Reactor*, NEDO-10174, 1977.

15. P. E. MacDonald, Personal Communication, EG&G Idaho, Inc., 1977.

16. F. Mayinger, *Nuclear Reactor Safety Heat Transfer* (Chapter 12), O. Jones (ed), Hemisphere Publishing Corp., 1981.